LONG RANGE MOIRÉ PATTERNS

BY

SAMUEL JOHN JOSEPH BANKS

Christchurch, New Zealand

sjb374@uclive.ac.nz

THESIS

In Partial Fulfilment

of the Requirements for the Degree of

Master of Engineering

MAY 2020

UNIVERSITY OF CANTERBURY

ABSTRACT

Previous work has gone towards using moiré patterns formed with lenticular lenses to perform pose estimation for short ranges. This thesis investigates existing theory of moiré patterns, most notably the Fourier and first harmonic approximation models. This theory has been drawn upon to create a generalised model of planar moiré patterns in 3D. For example, those generated from two patterns with fine grids separated in space. This improves on previous research that does not investigate this specific kind of 3D pattern as closely. This thesis also developed a framework that simulates moiré patterns using this model. Along with this, the proposed framework can also solve pose information about a moiré pattern given an image. Experiments varying camera lateral translation were accurate for the close-range testing, with about 10 mm accuracy from a distance of 160 mm. Results from varying camera distance where 0–130 mm accuracy varied from ranges 100–2000 mm. A y-tilt estimation experiment was performed using the solver from this framework. At 3.116 m it was able to estimate an angle with an error of 5° for angles as wide as 30° and was able to estimate angles with an error of 0.25° for angles less than 5°. This is better than similar existing methods such as the Metria Moiré Phase Tracking marker's maximum absolute errors of up to 2.8 mm and 2.1°.

ACKNOWLEDGEMENTS

Thanks to Richard Green, the project's University Supervisor, and Jun Junghyun, the project's Supervisor from Trimble, for the help and contributions to this work. Richard Green gave constant support and ideas to the project and Jun Junghyun helped guide the direction of the project and with performing the turntable experiments. Both helped with proofreading and feedback of this report.

Table of Contents

TABLE OF FIGURES

1. INTRODUCTION

The goal of this thesis is to attempt to utilize the phenomena that exist in moiré patterns and determine their aptitude for use in long-range positioning. To do so, theory is developed to model basic moiré patterns and some tests are carried out to determine some accuracies of this model. As well as get an idea of the improved accuracy the use of moiré patterns can bring. The specific questions this thesis was attempting to answer were, given a working range and required precision, what is the best choice of parameters of a moiré pattern; and, with patterns so sensitive to precision, can this be made accessible for an average user. That is, can the sensitivity be used to make a simple and easy to use, yet still accurate, marker. In pursuit of these questions, this thesis primarily focusses on developing and testing a model of 3D moiré patterns and using them to estimate pose information and determine the accuracy of it.

Moiré pattern's extra sensitivity to motion means that it has the potential to provide exceptional angle accuracy even for small almost planar angles. There is also potential for allowing improved distance estimation as well due to unique behaviours with certain types of patterns.

In this thesis, specific moiré pattern setups will be investigated to determine the kind of potentially achievable accuracies. These case studies aid to attempt to validate the model and provide a concept for an approach for using these patterns for positioning. However, the theory developed can model any moiré pattern that consists of multiple planar patterns whose patterns are representable as functions. The theory developed and experiments ran will also aid in providing some answers to the proposed questions.

This thesis also develops a MATLAB framework[1] for simulating these patterns and solving their positions in space given images of them. The MATLAB model is based on the analytic model developed in the paper. Due to the generalised model this MATLAB framework uses, it can simulate any type of moiré pattern generated from any number of planar grating patterns in any configuration. It provides the tools to create any such pattern of this kind and theoretically to solve any set of pose information, provided it is set up in a sufficiently constrained way.

This thesis looks specifically at moiré patterns generated by two planar grating patterns separated at a distance, such as in Figure 2. This will be the case study for applying and testing the developed model and MATLAB framework and for calculating the accuracy of estimates. Hence, some special cases of the general model are investigated in doing so.

---

[1]GitLab repository: https://gitlab.com/bankssa/moire-simulations

Contact e-mail provided for access.

1.1. *Moiré Patterns*

Moiré patterns are the phenomena that occur as a result of interference between two similar periodic patterns. This interference causes a more visually protenant tertiary periodic pattern that is not present in either of the two generating patterns. Figure 1 shows an example of a moiré pattern where overlaying two similar high frequency gratings causes a much lower frequency pattern to emerge. This new pattern becomes very sensitive to changes in either of the two superimposed patterns. Small shifts to the original patterns can cause large shifts in the interference pattern or even shifts in different directions or in other unexpected ways. As they shift, these emerging patterns can have all sorts of behaviours, such as the illusions of movement or depth [1]. If these patterns are set at a distance apart this interference pattern becomes sensitive to changes in viewing angle and viewing position, appearing to move as the viewpoint moves [2]. The main contribution of this report is in developing the Fourier and first harmonic approximation models of moiré patterns based on existing theory [3-9] and to apply to generating moiré patterns from two patterns set in 3D space at a distance from one another. The goal is to develop this model to estimate the position of a camera in space from a single image and investigate the accuracy of this model.

Figure 1: Moiré pattern generated from two colinear gratings with slightly different frequencies.

Specifically, this thesis's case studies use the investigated properties of moiré patterns to estimate a camera's *x*, *y*, or *z* position in space (in this thesis, the *x*-*y* position is referred to as lateral translation and the *z* position as distance) or to estimate the angle the moiré pattern is at about its *y*-axis, relative to the camera (called the pattern's *y*-tilt or tilt). These goals are summarised by Figure 2. This work focusses on the estimation of these parameters in individual test cases. The case studies of this thesis involve a lateral translation estimation case (estimating ΔX shift only), a distance estimation case (estimating d_1 distance), and a tilt estimation case (estimating *y*-tilt angle). But, theoretically, the support and tools of this thesis lend themselves to estimation methods that could potentially estimate all of these together; however, this would require creating new moiré pattern(s) with careful constraint consideration. The findings of these investigation are used to draw conclusions about how adept the use of moiré patterns is alone for long-range positioning, if these tests show the model is capable of determining the best moiré pattern parameters for a working range, and if the method is accessible to a normal user.

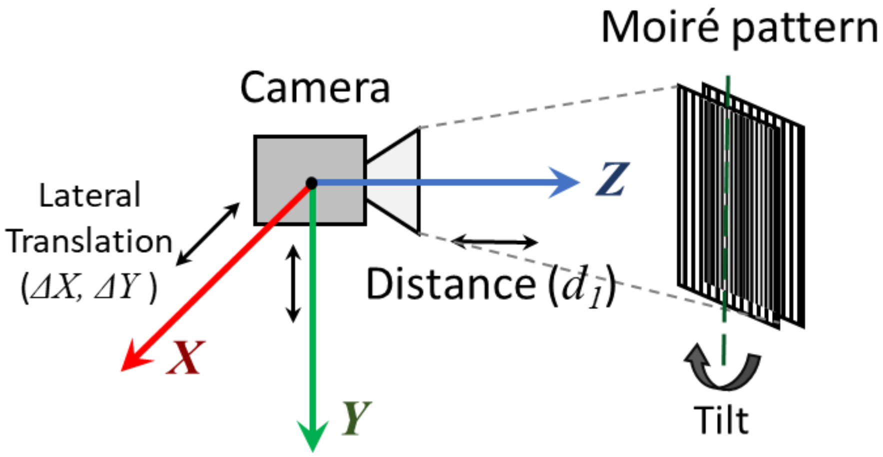

Figure 2: Cases study setup use in investigating the quations of this thesis.

The main advantage this method of positioning has over other marker-based photogrammetric methods, such as using fiducial markers, is that it does not require precise camera calibration. However, precisely setting up the pattern itself can be necessary depending on the accuracy desired. The general sensitivity of moiré patterns, however, make it both easier to construct them with reasonable accuracy by hand and allow there to still be good accuracy even if it is constructed imperfectly. The nature of moiré patterns, however, can lead to small imprecisions having quite varied effects on how it affects precision. A pattern may still be accurate, say, head-on, but accuracy may “drift” as the pattern reaches its extremes (say, an extremely steep tilt angle). There is also a great future potential that moiré-based markers could be made more accurate than traditional photogrammetric methods due to their unique sensitivity. If this could be achieved, it could potentially greatly surpass existing methods while still maintaining relative simplicity and usability for a normal user.

1.2. Contributions

- Unique look specifically at moiré patterns created from multiple planar grating patterns in 3D
- A full model of 3D planar moiré patterns
- Verified this model through experimentation
- Created a MATLAB framework available in a GitLab repository
    - Implements the developed moiré theory
    - Provides visualisation tools
    - Developed a solver for pose-finding moiré patterns from camera images
    - Includes a repository of labelled ground-truth images of these moiré patterns
- Investigated how to design these types of patterns for a specific application
- Investigated the accuracies using these types of moiré patterns
- Published a paper on this topic at an IVCNZ conference

2. BACKGROUND

The word "moiré" comes from the French word "moiré", meaning "watered". The name "moiré" pattern comes from being named after a French textile of the same name [10]. This fabric was made of two pieces of silk with fine patterns fixed together, one over the another, causing an intricate wavy "watered" interference pattern. Hence giving rise to the name of the moiré phenomenon where two similar patterns interfere to cause a third emerging tertiary pattern. Moiré patterns crop up in a vast number of varying places and have lots of very interesting and counter-intuitive properties [11]. Sometimes this moiré effect is sought after, perhaps for visual purposes. For example, [12] investigates the effects of moiré patterns caused by superimposing a lenticular plate in front of an LCD screen such that different patterns are seen from different viewing angles. The effect of separated generating patterns is also investigated. Dubbed "2.5-D" displays, the use cases discussed are for billboards or advertisements to make a more interesting display that changes with viewing angle and distance. Other work has also gone into investigating moiré patterns to intentionally avoid them occurring [13], or to utilise them for artistic or visual reasons. Like in [14], where the intricate moiré images that can form when transparent sheets with regular patterns are laid on top of one another are utilised to make interesting patterns that move when one of the sheets are moved. Depending on the patterns, this can cause all sorts of interesting interference patterns, being incredibly sensitive to shifts in either sheet. Weird results such as forming microstructures, moiré pattern rotation, scaling, and translation can appear. [14] uses these interesting behaviours and sensitivities to shifts in the sheets to specifically design moiré patterns which show specific images or text that reveal themselves or appear to move or animate as the top sheet is shifted, such as those shown by Figure 3.

Figure 3: Example of text resulting from the microstructures of moiré patterns [14]. As the top black sheet is shifted, the word "UNO" and the red bands appear to shift up and down.

These unique and interesting properties of moiré patterns have made them useful in a wide variety of applications, such as displacement measurement, refractive index gradient measurement, interferometry, and others [15-19]. For example, moiré patterns have been used in past for use in surface imaging and contouring [20, 21]. One practical example of moiré patterns being uses this way is to look at the geometry of a person's back to be able to find back deformities such as scoliosis [22, 23]. This requires capturing how a grid projected onto a surface interferes with another grid pattern (typically itself) in order to determine the contour of the surface, and hence, in this case, evaluate the spinal deformities of a patient. Figure 4 shows an example of a moiré pattern being used to image a patient's back by the way the interference creates an elevation height-map–like pattern on their back. This is achieved by projecting a grating pattern onto a patient's back and using the natural interference of the projection and the grating casting the projection to determine height information about the patient's back. This involves modelling how two periodic patterns interfere at a distance, where one pattern is deformed across a surface. This thesis focusses on a similar case of moiré pattern, except where the second grating, the one cast on the patient, in this case, is simply another flat grating pattern and can be different to the first in frequency. And with a different goal of positioning in mind.

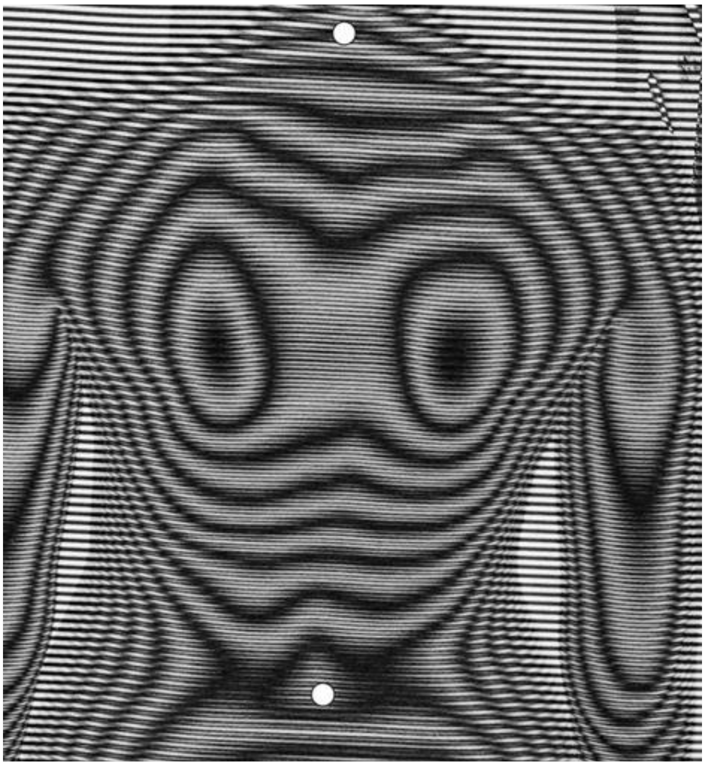

Figure 4: Moiré patterns being used to image spinal deformities [22].

Another example where moiré patterns can form with weird behaviours is by positioning a lenticular lens above a grating pattern such as those explored in [24]. Figure 5 shows such an interference pattern caused by a lenticular lens placed at a separation from a grating pattern. Rotating, shifting, and raising the lenticular lens causes different resulting patterns to emerge as a result.

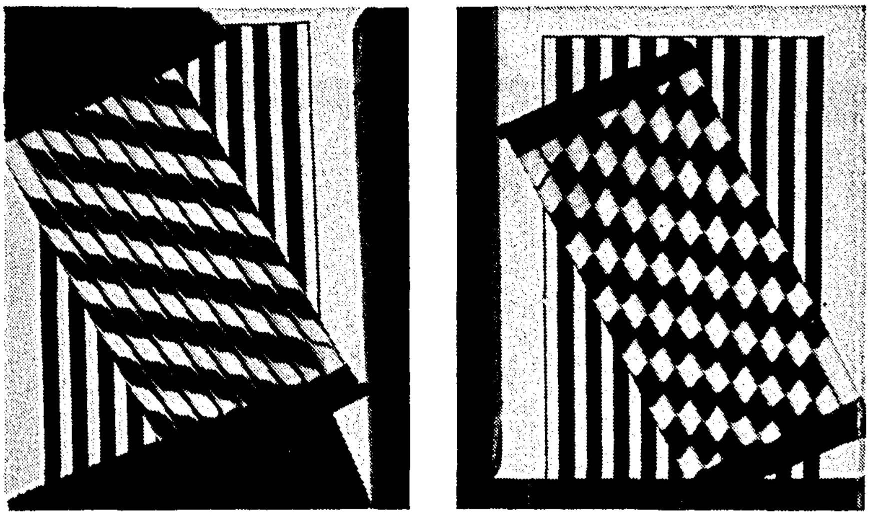

Figure 5: Interference moiré patterns caused by positioning a lenticular lens over a grating pattern with different separations [24].

This behaviour with lenticular lenses is one that has been primarily utilised in several other mark-based positioning solutions that augment themselves with traditional fiducial marker–based positioning. Moiré patterns in markers like this also have lots of potential for robotics applications, in the many applications that are typically achieved with fiducial markers [25]. Marker-Based tracking is important in many other areas as well, such as for machine positioning [25] and calibration [26], augmented reality (AR)[27], virtual reality, and grade control. Many solutions for positioning without the use of moiré patterns already exist. Including non-passive approaches, and simple passive marker detection such as fiducial markers. These non-passive approaches have the issue that they require special equipment or special cameras to get high accuracy. For this reason, in many cases, simple marker-based solutions, such as the use of fiducial markers, are often used instead. Many kinds of fiducial markers exist, including ARToolKit, ARToolKitPlus, ARTag, and AprilTag[28-31]. Decently high accuracy can be achieved with fiducial markers [32], but their accuracy is still limited and breaks down specifically for distance estimates and small-angle estimation when the marker is almost planar to the camera and can also require great camera calibration for high accuracies. Effort has gone toward trying to solve the pose ambiguities that arise in these situations [33]. Fiducial markers and some other approaches also have the downside that they don't work well at very long distances greater than about 5 metres [34]. Previous work has already gone toward incorporating moiré patterns into existing fiducial marker–based solutions for positions, such as the use of more accurate fiducial markers in AR [35]. Such an example is the LentiMark [36] marker shown in Figure 6, integrating moiré patterns created via the use of lenticular lenses with the existing fiducial marker ARToolKitPlus [29].

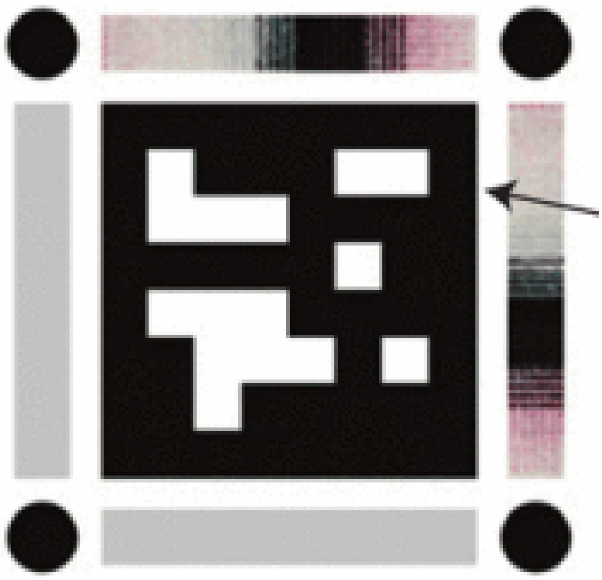

Figure 6: LentiMark pattern incorporating a fiducial marker (shown by arrow) and lenticular-based moiré patterns [36].

These markers work by using the existing fiducial marker to both detect and locate the marker and provide an approximate pose for the marker. The lenticular-based moiré patterns on the edges are then used to further refine the pose estimation. It does this by detecting where the two distinct fringes are positioned relative to their pattern on two different axes. This helps refine pose information for both *x* and *y* rotation of the pattern, the type that is most difficult to get accurately using a fiducial marker.

Most of these applications would benefit from or have applications in being able to perform more accurately or in long-range positioning. These existing marker-based solutions are not suited for these longer ranges, however. Other solutions for positioning exist such as non-passive sensor methods, which are often used when these high accuracies at long ranges are desired. However, fiducial markers don't work at very long ranges, and decrease significantly in accuracy for distance and angles when viewed head-on. This is due to the reduced sensitivity of changes in an image when a fiducial marker moves or rotates when viewed head-on. Work has gone into attempting to design fiducial markers that work at longer distances, but this is mostly for indoor purposes. Even so, these working longer ranges are only from 1250 mm to 5000 mm and are required to be large (at 20 cm × 20 cm). These are also subject to poor detection under motion-blur [34].

Moiré pattern–based markers have the potential to be much less affected by motion-blur as the pattern of interest in a moiré pattern is of low frequency. Motion-Blur theoretically may even improve the detection of these frequencies. This lower-frequency pattern detection also makes them easier to be recognized at longer ranges, as well as the added longer-range accuracies they can provide due to their sensitivity.

2.1. Relavant Papers

There are existing fiducial markers that incorporate moiré effects to improve pose estimation of the marker. Other moiré tracking techniques have an advantage on other markers [37], getting higher accuracy. This primarily significantly improves rotation estimation; however, distance estimation is not as accurate. These types of markers can be achieved in a few ways. Either by small scale separation of periodic patterns or using lenticular lenses. Lenticular lenses magnify different parts of a printed image when viewed from different angles. The moiré interference is achieved by having the frequency of the pits of the lenticular lens slightly offset from the printed image of a grating. This can induce moiré patterns, adopting the same sensitivity to viewing angle [36]. One such marker incorporating this effect is Metria's Moiré Phase Tracking Markers [38]. These can be purchased as a part of a kit provided by Metria which already comes with the pose estimating software. They achieve this by looking at the phase difference of several moiré patterns on a target that all change differently to position and rotation. However, these markers have their limitations. Most notably, these markers work optimally at a limited distance with an accuracy of 1.0 mm at distances less than 2.5 meters.

Theories of moiré pattern interference, in general, have been investigated. Many methods of capturing the moiré phenomena exist, including the indicial, Fourier, first harmonic approximation, and parametric models, as well as others [3-9]. [3] itself is a very useful resource going over general theories and considerations of moiré phenomena. It has an emphasis on the benefits of the Fourier model as well as considerations and evaluations for other methods. Some of these models are considered and evaluated here as well. The basis for the theory developed in this thesis is determined to be the first harmonic approximation model, which is a simplification of the Fourier model. Although there are moiré phenomena that are not entirely explainable by the Fourier model [39], these are fringe cases and it is more than suitable for types of moiré patterns explored here.

2.2. Moiré Phase Extraction

There was also been other similar work instead toward extracting phase information of moiré targets [40]. This work was instead looking at circular moiré patterns formed via concentric ring structures on a film, called a Fresnel Zone plate. An example of the Fresnel Zone plate is shown in Figure 7.

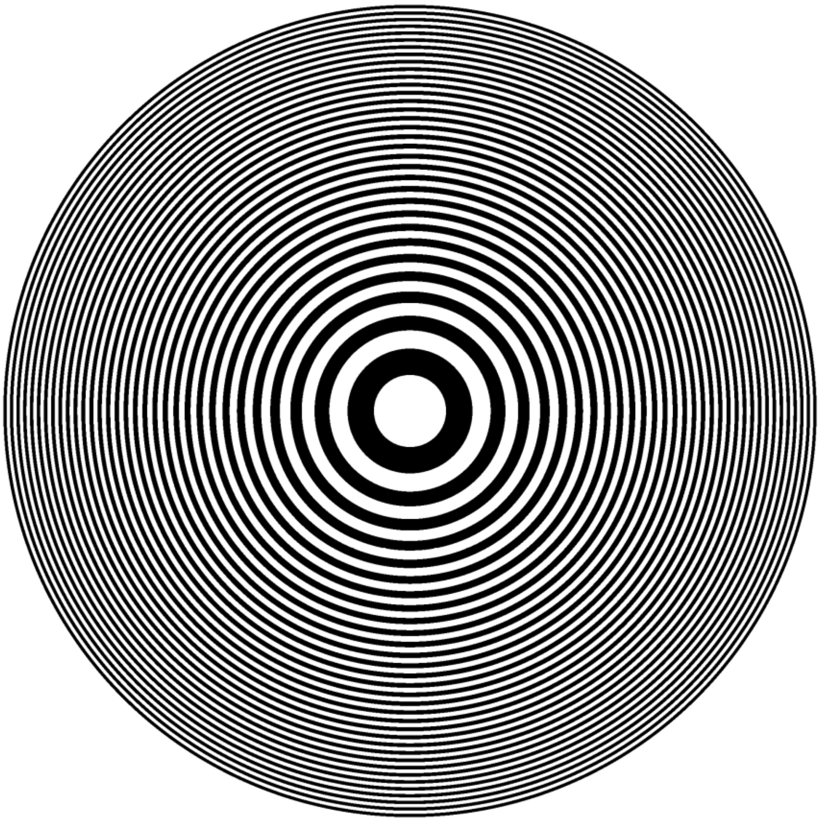

Figure 7: An example of a Fresnel Zone plate [40].

This grating film was placed in front of a reflector and the interference moiré pattern that emerged was investigated and mathematically modelled by use of the Windowed Fourier transform and Herbert transform. A rough schematic of this type of moiré target is shown in Figure 8. A marker like this has the capacity for high accuracy for finer straight-on rotations but fails for particularly wide angles. It also does not perform well at long ranges due to the small intricate design.

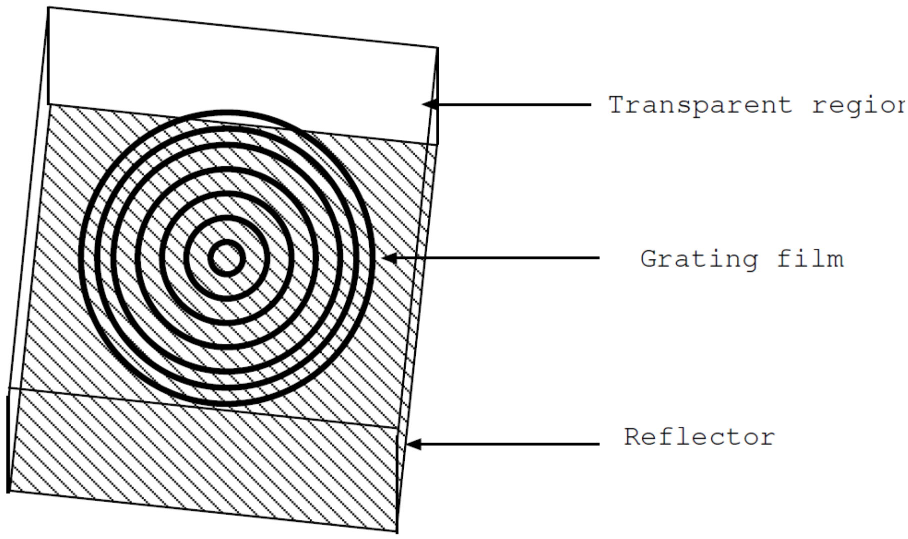

Figure 8: Schematic diagram of the moiré targets investigated by [40].

This model was used to model and extract phase information about the moiré pattern from photographs. A similar overall method has been carried out here, where a specific type of moiré pattern setup has been investigated and modelled. However, in the case of this paper, the goal is to directly estimate and model pose information of the moiré pattern from the camera images. Most specifically the relative angle of the pattern to the camera (the tilt), however a concept for distance estimation is also investigated. A shortcoming with this research is that although fundamental moiré theory is discussed and used, the developed model is limited to the overlapping concentric ring structure–type moiré patterns. This thesis aims to model arbitrary 3D planar moiré patterns.

2.3. Indicial Model

Varying theory exists to model basic moiré interference, each with different strength and weaknesses. One is the indicial model, described in [9], which discretises the periodic patterns as a series of indexed lines. Pairs of patterns can then have their interference represented in terms of these indices, creating a new indicial model that represents the interference. Different modes of interference can be calculated, however, there is no way to determine the prominent mode of interference (which is perceived). The mode of a two-pattern moiré is written as a (k_1, k_2)-moiré, where k_1 and k_2 are integers. The indicial model then relates the indices of the two patterns (n and m) to the indices of the moiré pattern (p) as shown in Equation 1, where n, m, and p are all integers.

$$k_1 n + k_2 m = p \qquad (1)$$

If the two patterns are both linear patterns (made strictly of lines separated periodically) at an angle, then they can be represented as indexed lines equations on an xy-plane. This is shown by Equation 2 and Equation 3, where pattern one is index by n and has a period of T_1, and pattern two is index by m, has a period of T_2, and is rotated from pattern one by θ counter-clockwise.

$$x = nT_1 \tag{2}$$

$$x\,cos(\theta) + y\,sin(\theta) = mT_2 \tag{3}$$

From this, the line index form of the resulting moiré pattern caused by the interference of these two generating patterns for the $(1, -1)$-moiré can be determined, shown in Equation 4.

$$\frac{x}{T_1} - \frac{(x\,cos(\theta) + y\,sin(\theta))}{T_2} = p \tag{4}$$

Then each index in p represents a band in the $(1, -1)$-moiré pattern formed from the interference between the two generating patterns. This theory can also be expanded to incorporate arbitrary numbers of generating patterns as well as represent other nonlinear types of patterns representable by functions. Figure 9 shows visually the representation of the indicial model, showing a $(1, -1)$- and $(1, -2)$-moiré interference patterns, as well as how this model would work for nonlinear generating patterns.

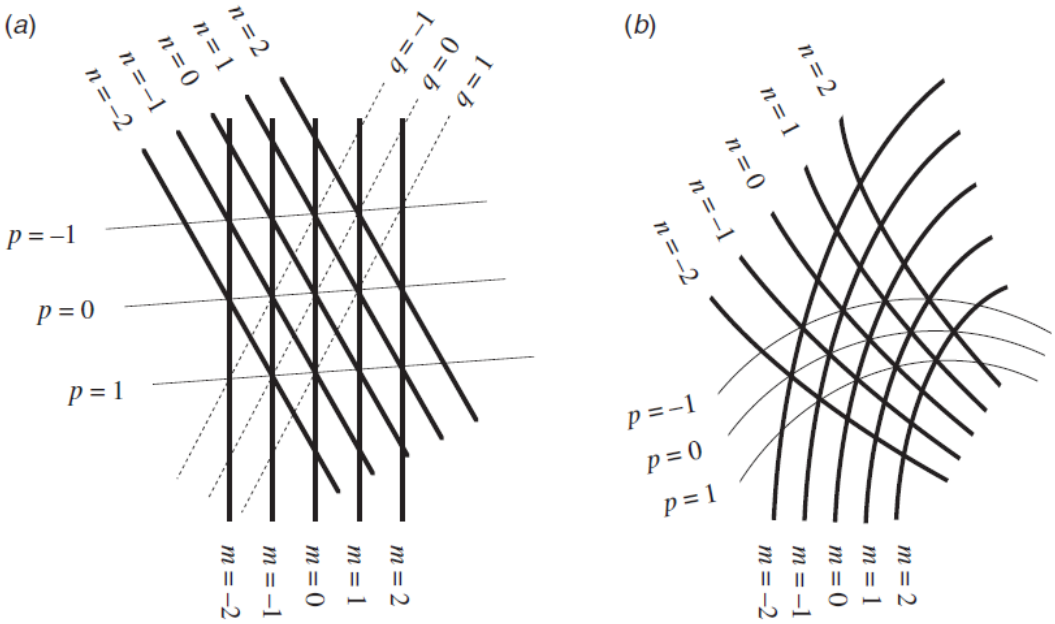

Figure 9: Depiction of the indicial moiré model. n and m are the line indices of the generating pattern, p is the line index for a (1, −1)-moiré, and q is the line index for a (1, −2)-moirė. a) shows the model for the interference of linear patterns; b) shows the model for the interference of curvilinear patterns. Figure from [9].

The indicial model is a more computationally efficient model capable of representing interference of linear and some nonlinear patterns; however, it is limited to representing patterns as a series of lines not considering line thickness or pattern intensity. This model is also entirely encapsulated in the Fourier model, providing a strict subset of the analytical power that the Fourier model does. The indicial model also does not give a way to know which mode of the moiré pattern is the most visually prominent. The indicial model does still serve as a useful basic intro to moiré pattern behaviours and theory expanded on by the Fourier model, such as the mode of a moiré interference pattern.

2.4. Fourier Model

The Fourier model is a more comprehensive model that captures more of the behaviour of moiré interference. However, it is more complicated and computationally expensive than other models. But it does give a fuller picture. The Fourier model works by considering the spectral decomposition of the generating patterns and modelling how they interact and looking at the resulting spectral pattern for signs of moiré interference.

The act of overlaying patterns can be modelled either as multiplicative or as additive. It may appear natural to assume that overlaying patterns interferer additively, or as an average, allowing an amount of light through equal to the average of the light that would pass through the original patterns. This is a reasonable enough assumption to get meaningful result that can be used to analyse the patterns carrying out analysis purely in the image domain. However, it is more natural to conceptualise the interference as multiplicative, as is the primary focus of [3, 41]. With this model, a value of zero indicates that no light can pass through, and a value of one indicates that all the light can pass through. In [3], this is called the transmittance of the pattern. Hence if all overlaying parts of a pattern allow light to pass, their product also allows light to pass. And if any one of the overlaying parts of a pattern does not allow light to pass through, their product will not allow light to pass through. This gives the desired interference behaviour. Analysing the Fourier spectral decompositions of generating patterns alongside their moiré interference pattern, the frequencies of the moiré pattern become clear. An example of this is shown in Figure 10. Note that the Fourier model interprets (k_1, k_2)-moiré patterns modes as having a frequency of $k_1\boldsymbol{f_1} + k_2\boldsymbol{f_2}$, where $\boldsymbol{f_1}$ and $\boldsymbol{f_2}$ are the frequency vectors of the generating patterns. A frequency vector as a magnitude equal to the frequency of a grating and a direction pointing in the direction the grating is orientated (perpendicular to its grating lines). A $(1, -1)$-moiré pattern is shown to arise in the example of Figure 10.

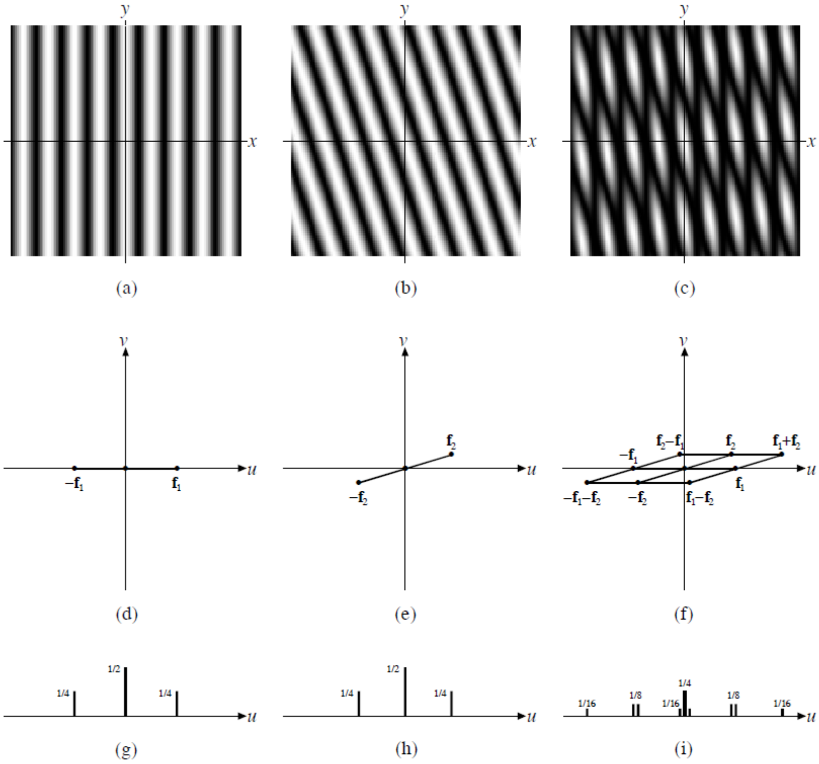

Figure 10: Two sinusoidal patterns a) and b) and their overlaid pattern c). d), e), and f) are the respective Fourier decompositions showing the frequency locations in 2D; and g), h), and i) are the respective Fourier decompositions showing the impulse amplitudes. Figure from [3].

With an additive model, no other frequencies show in a Fourier analysis outside of the original frequencies, and the beat frequency in the image must be investigated directly to draw meaningful conclusions. However, this analysis can still be taken to draw some of the same conclusions but shows a less full picture. For this reason, focus will be on the multiplicative model, as was done in [3]. Notice that figure f) of Figure 10 is the convolution of d) and e) of Figure 10. This reflects the fact that multiplication in the image domain corresponds to convolution in the Fourier domain. This is the key property that causes the moiré frequencies to appear in the Fourier transform using the multiplicative model. This method also provides an easy method of determining what modes of moiré pattern are likely to be visible. In general, the lower the frequency of a moiré pattern, the more prominent it is to the human eye. [3] drew a circle around the origin and call it the "visibility circle," indicating the range of lower frequencies at which a moiré pattern is seen.

2.5. First harmonic approximation model

The first harmonic approximation model involves taking only the primary frequency component of the generating patterns and the moiré pattern. This first-order frequency approximation of a 2D grating represented on the *xy*-plane and rotated by and angle θ_1 is shown by Equation 5, where f_1 is the fundamental frequency of the grating. This is a transmittance function, $P_1(x, y)$, of x and y of which parts of the pattern allow light to pass through.

$$P_1(x, y) = \frac{1}{2} + \frac{1}{2} cos\big(2\pi f_1(x\, cos(\theta_1) + y\, cos(\theta_1))\big) \quad 5$$

Alternatively, this can be put in a vector form, shown by Equation 6, with $\boldsymbol{f_1} = [f_1 \cos(\theta_1), f_1 \sin(\theta_1)]^T$ and $\boldsymbol{x} = [x, y]^T$, where the transmittance function is now written $P_1(\boldsymbol{x})$.

$$P_1(\boldsymbol{x}) = \frac{1 + cos(2\pi \boldsymbol{f_1} \cdot \boldsymbol{x})}{2} \quad 6$$

Overlaying two generating patterns, hence multiplying them, this becomes Equation 7.

$$P_1(\boldsymbol{x}) = \frac{1}{4}\big(1 + cos(2\pi \boldsymbol{f_1} \cdot \boldsymbol{x}) + cos\big((2\pi \boldsymbol{f_2} \cdot \boldsymbol{x})\big) + cos(2\pi \boldsymbol{f_1} \cdot \boldsymbol{x})\, cos(2\pi \boldsymbol{f_2} \cdot \boldsymbol{x})\big) \quad 7$$

The using trigonometry rules and the properties of the dot product, this becomes Equation 8.

$$\begin{aligned} P_1(\boldsymbol{x}) = \frac{1}{4} + \frac{1}{4} cos(2\pi \boldsymbol{f_1} \cdot \boldsymbol{x}) + \frac{1}{4} cos(2\pi \boldsymbol{f_2} \cdot \boldsymbol{x}) + \frac{1}{8} cos(2\pi (\boldsymbol{f_1} - \boldsymbol{f_2}) \cdot \boldsymbol{x}) \\ + \frac{1}{8} cos(2\pi (\boldsymbol{f_1} + \boldsymbol{f_2}) \cdot \boldsymbol{x}) \end{aligned} \quad 8$$

Where the first term is the DC component, the second and third terms the original frequencies of the generating pattern, and the fourth and fifth terms correspond to the frequency components of the (1, −1)- and (1, 1)-moirés respectively. In practice, with generating frequencies that are very similar the (1, −1)-moiré and DC components contribute most to the visible pattern observed as the other frequencies lie outside of the visibility circle [3]. Therefore, only the first and fourth terms are needed to approximate the moiré pattern, giving Equation 9.

$$P_m(\boldsymbol{x}) = \frac{1}{4} + \frac{1}{8} cos(2\pi (\boldsymbol{f_1} - \boldsymbol{f_2}) \cdot \boldsymbol{x}) \quad 9$$

This gives an equation which represents the overlaying moiré pattern while still maintaining the intensity component. The cosine term can be investigated on its own if the only interest is the frequency of the moiré pattern. The advantage of this approach is that it is algebraic and therefore simple algebraic manipulations and modifications can be made and their implications simply mechanically carried out. Such as if the frequency of a generating pattern depended on $\boldsymbol{x}$, this could be injected algebraically. You also maintain some intensity information with this approach. However, you lose some of the elegance and generality given by the Fourier approach, as this approach is fully encapsulated in the Fourier approach.

2.6. Evaluation

Previous marker-based solutions are limited in one way or another or even rely on being incorporated with existing technologies such as fiducial makers.

No models so far incorporate the effects of patterns separated by a distance in 3D for arbitrary planar patterns. However, a model can be developed based on the theory of [3]. The first harmonic approximation model provides the flexibility to investigate the implications of a separation between the two patterns. Simple transformations to scale the patterns based off their distance from a camera can be done to model a pinhole camera model. Then the interference can be calculated as normal. This becomes more complex of a task for arbitrary planar patterns in space that aren't planar to the camera but can still be done starting from this model. The indicial model falls short in the difficulty of adapting and changing it to model separated patterns like is desired. The Fourier model could also have been chosen to develop the solution; however, it was ultimately decided that the simpler nature of the first harmonic approximation model was easier to work with. Therefore, this thesis will aim to develop a model of the types of moiré patterns investigated from the ground up based upon previous existing theory of the moiré pattern phenomenon.

3. Proposed Method

A model was developed from previous research to represent the moiré phenomenon. This model was then used to create a MATLAB simulation that could simulate various planar moiré patterns. Several experiments were then run to both determine the accuracy of this simulation and its ability to determine pose information about photographs of moiré patterns and to attempt to determine the aptitude of the use of moiré patterns for long-range positioning.

The experiments in this thesis are represented in 3D space. There's a fixed camera at (0, 0) with its optical axis pointing along the z-axis. In front of it is a moiré pattern consisting of several overlapping grating patterns in 3D space. A grating pattern is a pattern with a simple grid pattern with alternating dark opaque and transparent stripes, as shown by Figure 11, with a separation (p) or frequency ($f = 1/p$) parameter, as well as a grating thickness parameter, which is typically 50%.

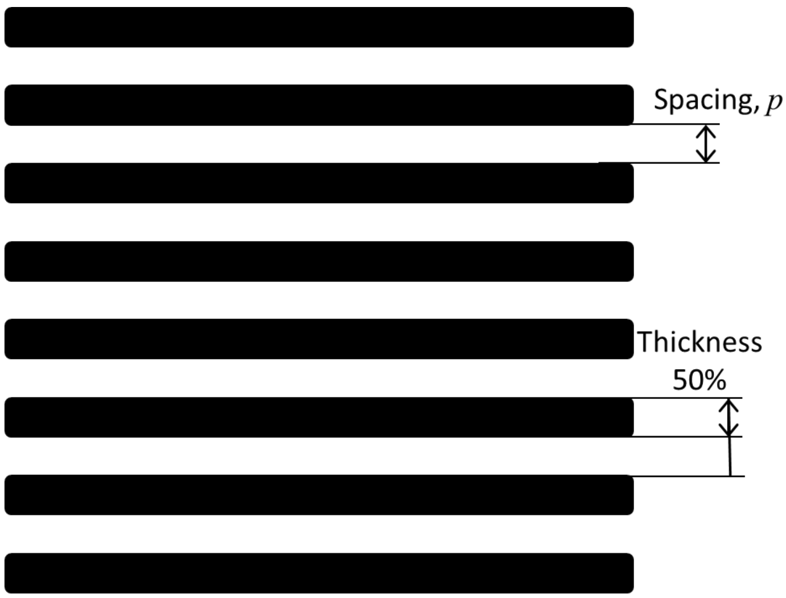

Figure 11: An example of a grating pattern and its parameters.

Overlapping in the context of projection means that portions of each grating pattern individually map to the same location in the camera's image. This is what causes a moiré pattern to form. Figure 12 shows an example with only two grating patterns. This was numerically simulated in MATLAB. To model this mathematically, the grating patterns are modelled as simple sinusoidal functions. Reverse projection also needs to be performed to determine the point on the pattern function in 3D space that corresponds to a given point in the camera image. This needs to be done for all grating patterns. After this, the moiré interference theory can be incorporated to generate the model of the moiré pattern. Two models were developed in this thesis to achieve this. The first was an initial model created more directly from previous work. This model was then expanded upon to create a more useful general model. This model has fewer restrictions on the types of planar moiré patterns it can model.

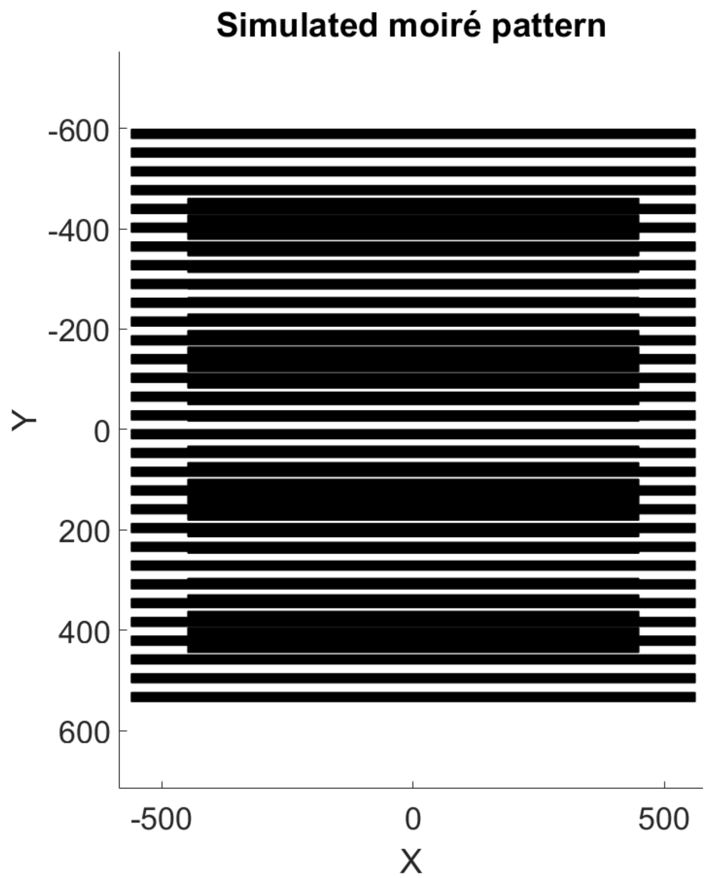

Figure 12: Numerically simulated image of 3D planar moiré pattern.

A MATLAB framework was developed to simulate these planar moiré patterns. This framework performs numeric and analytic simulation. The numeric simulation helps with creating visualisations of pattern setups for more visual direct comparison to the same real-world setup. The analytic model uses the generalised theory developed and is used to generate simulated images to feed into a solver (which also takes true images) to determine the pose of the pattern. The types of images the analytic model generate can be directly compared to true images, whereas the numeric simulation cannot (as all geometry is represented as vectors with this type of simulation).

3.1. Initial Model

The initial theory proposed was to expand upon the theory from [3] to account for separation between moiré patterns. This will only focus on moiré patterns between two patterns. Multiple bases from [3] that can be used in developing these new equations. The key takeaways will be investigating how moiré interference changes as the camera moves in space. Theory will be developed based on the first harmonic approximation method proposed by [3]. The gratings, then, can be represented by Equation 6.

$$P_1(\boldsymbol{x}) = \frac{1 + cos(2\pi \boldsymbol{f}_1 \cdot \boldsymbol{x})}{2} \tag{6}$$

And similarly, for pattern two. To model the fact the patterns are separated, both patterns are scaled, undergoing a pinhole camera projection, based on their distance from the camera. For example, with pattern one, this involves scaling the parameter $\boldsymbol{x}$ by d_1/f to represent pinhole projection, where f is the focal length of the camera and d_1 is the distance pattern one is from the camera in the z-axis shown in Figure 2 (the optical axis of the camera). Pattern one is considered as the pattern closest to the camera. However, to simplify this, the scaling will be incorporated into $\boldsymbol{f_1}$, labelling this $\boldsymbol{f_{s1}}$, as shown by Equation 10.

$$\boldsymbol{f}_{s1} = \frac{d_1 \boldsymbol{f}_1}{f} \tag{10}$$

And similarly, for pattern two to get $\boldsymbol{f_{s2}}$. However, pattern two's distance will be defined as $d_2 = d_1 + d$ for some z-separation between pattern one and pattern two of d. Overlaying the projected patterns one and two, corresponding to multiplying them [3], and leaving only the visible components as discussed in Section II D, results in Equation 11, a transmittance function representing the moiré pattern, $P_m(\boldsymbol{x})$.

$$P_m(\boldsymbol{x}) = \frac{1}{4} + \frac{1}{8} cos(2\pi(\boldsymbol{f}_{s1} - \boldsymbol{f}_{s2}) \cdot \boldsymbol{x}) \tag{11}$$

This corresponds to the (1, −1)-moiré interference pattern as described by [3]. This shows the limitation to the first harmonic approximation of the pattern as it ignores the possibility of other modes of moiré pattern formation. However, one can ensure that the (1, –1)-moiré will always be the most prominent moiré, typically by choosing two patterns with sufficiently similar frequencies.

This gives the frequency of the resulting moiré pattern, $\boldsymbol{f_m}$, as $\boldsymbol{f_{s1}} - \boldsymbol{f_{s2}}$. Equation 12 shows this in its expanded form, with $\theta_2 = 0$.

$$\boldsymbol{f_m} = \boldsymbol{f}_{s1} - \boldsymbol{f}_{s2} = \begin{bmatrix} f_{s1}\, cos(\theta_1) - f_{s2} \\ f_{s1}\, sin(\theta_1) \end{bmatrix} = \frac{f_1}{Df} \begin{bmatrix} d_1 D\, cos(\theta_1) - d_2 \\ d_1 D\, sin(\theta_1) \end{bmatrix} \tag{12}$$

Defining D as f_1/f_2. Note that, with a non-zero θ_1, the angle and magnitude of the moiré pattern's frequency change with distance d_1. With zero θ_1, only the frequency vector's magnitude changes. Equation 13 captures how the moiré pattern's angle changes with distance, d_1, where θ_m is the angle of the moiré pattern in the camera image.

$$\tan(\theta_m) = \frac{d_1 D \sin(\theta_1)}{d_1 D \cos(\theta_1) - d_2} \quad 13$$

This shows a hyperbolic relationship between the slope of the moiré pattern and the distance of the pattern, d_1. This corresponds to the fact that at some d_1 the angle of the moiré will be 90°, vertical. This also means that the moiré angle is much more sensitive around such a d_1, which can be used in designing a pattern that needs to be more sensitive to a certain range. There is also a need for a separation and relative rotation between the patterns, otherwise distance has no effect on the slope of the moiré pattern. Rearranging to find d_1, noting $d_2 = d_1 + d$, this becomes Equation 14.

$$d_1 = \frac{-d \tan(\theta_m)}{D \sin(\theta_1) + (1 - D \cos(\theta_1)) \tan(\theta_m)} \quad 14$$

Therefore, with a known separation, relative frequencies, and non-zero angle between the generating patterns, the distance the camera is from the patterns can be estimated. Also, note that this does not depend on camera focal length.

From this, the frequency of the moiré pattern on the image has been calculated and can be used to determine how changes in viewing distance and camera panning affects the moiré pattern. To incorporate camera lateral translation, the following changes need to be made, shown in Equation 15, where $\boldsymbol{\Delta X} = [\Delta X, \Delta Y]^T$, of some shift in x and y.

$$P_1(\boldsymbol{x}) = \frac{1 + cos(2\pi \boldsymbol{f}_1 \cdot (\boldsymbol{x} + \boldsymbol{\Delta X}))}{2} \quad 15$$

Following the same process as before, this leads to Equation 16, where $\boldsymbol{f_d} = \boldsymbol{f_1} - \boldsymbol{f_2}$.

$$P_m(\boldsymbol{x}) = \frac{1}{4} + \frac{1}{8} cos\big(2\pi(\boldsymbol{f_m} \cdot \boldsymbol{x} + \boldsymbol{f_d} \cdot \boldsymbol{\Delta X})\big) \quad 16$$

From this, it can be observed that camera lateral translation purely contributes to the phase of the moiré pattern. If pattern one's and pattern two's frequency vectors are collinear ($\theta_1 = 0$), this can be used to determine pure x-translation of the camera, ΔX. In this case, there is no y contribution for any of the parameters, and therefore each parameter is simply represented as a scaler. With some rearranging, this gives Equation 17, where δx is the x-offset of the centre fringe of the resulting moiré pattern. Non-bolded terms represent the magnitude of their corresponding vector terms (which is purely their x-component in this case).

$$P_m(x) = \frac{1}{4} + \frac{1}{8}\cos\left(2\pi f_m\left(x + \frac{f_d}{f_m}\Delta X\right)\right) = \frac{1}{4} + \frac{1}{8}\cos\big(2\pi f_m(x + \delta x)\big) \quad 17$$

Since δx can be measured directly from an image, lateral translation, ΔX, can be calculated using f_d and f_m. Equation 18 shows how to calculate this lateral translation, where p_m is the measured separation between peaks of the moiré pattern (inverse of f_m), and p_d is the inverse of f_d.

$$\Delta X = \frac{\delta x f_m}{f_d} = \frac{\delta x p_d}{p_m} \quad 18$$

This can also be calculated without needing to know the camera's focal length. Note that the offset in the moiré pattern can only be measured mod p_m and as such this limits this method's ability to estimate camera lateral translation to values mod p_d. This can be overcome if the same fringe is persistently tracked, but that is not always possible if the fringe moves outside the moiré pattern. However, it is feasible that the position of the fringe, in this case, could be extrapolated from the visible part of the pattern. However, these methods require inter-frame processing, and this thesis is only concerned with single-frame processing.

3.2. Generalised Model

After experiments were run with the previous model to determine if it was correct or not, it was expanded upon to be more general. This generalised model builds upon the previous model, taking its core concepts and generalising some of them. An overview of the steps is as follows. Any number of patterns in 3D space can make up the moiré pattern. Each of these patterns are represented as a function (a sinusoid) on a 2D plane (its pattern plane). Each of the patterns need to have its function projected onto the image plane; to do so, the image planes coordinates need to be "reverse projected" and mapped onto each of the pattern planes. This mapping is then used to perform the Fourier moiré interference theory as before to calculate a function in the image plane of the moiré pattern.

3.2.1. Reverse Projection

Reverse projection is done by mapping an image point's *x*-*y* location to a pattern plane's *r*-*s* location. Figure 13 and Figure 14 show what is meant by reverse projection, where the black pyramid is the camera and its camera plane (the *x*-*y* plane), and the blue plane is the pattern plane (the *r*-*s* plane). The black line coming out of the back of the blue plane is its normal vector. The green line is a ray projected from the camera to the pattern plane at some point (the blue x), the red x indicating where this pattern's point is projected to in the camera image. The red lines are the *x* and *y* coordinates of the point on the image plane, and the blue lines are the *r* and *s* coordinates of the point on the pattern plane. The goal is to perform this projection from the pattern plane point to the image plane point (the normal direction of projection) in reverse; that is, to be able to calculate the pattern plane coordinates (r, s) from a coordinate point on the image plane (x, y).

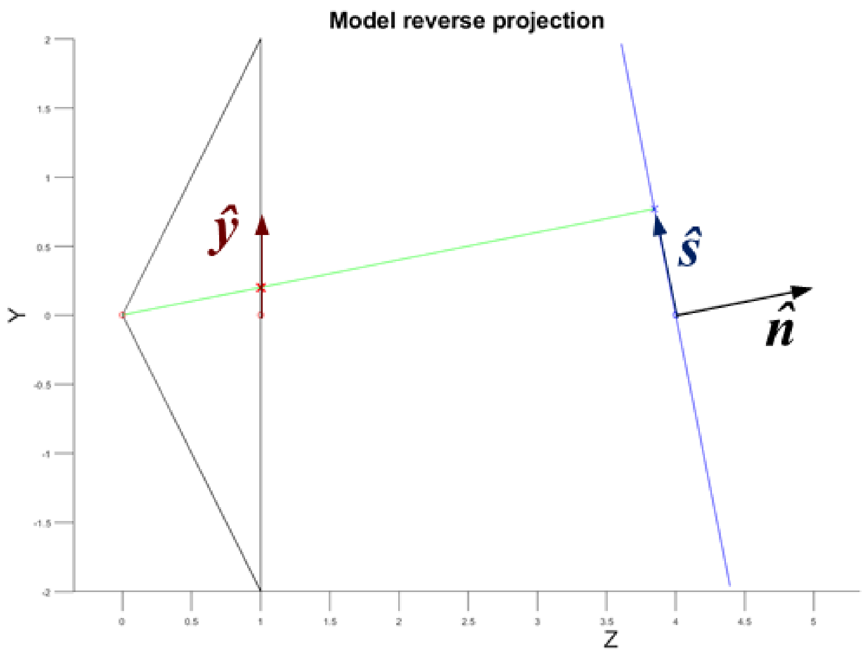

Figure 13: Side view of reverse projection (green line) from the x-y image plane to the r-s pattern plane.

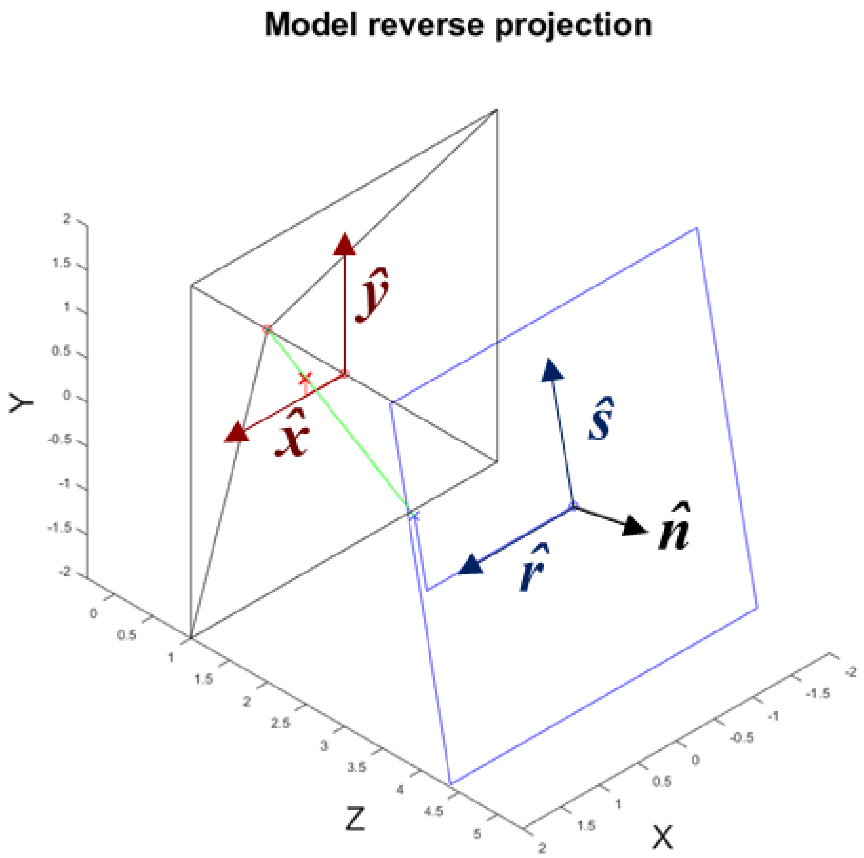

Figure 14: Three-quarters of reverse projection (green line) from the x-y image plane to the r-s pattern plane.

A pattern plane is therefore defined by the directions of its *r*- and *s*-axis vectors. These are labelled $\hat{\boldsymbol{r}}$ and $\hat{\boldsymbol{s}}$. The normal vector of the plane, $\hat{\boldsymbol{n}}$, can be calculated from the cross product of $\hat{\boldsymbol{r}}$ and $\hat{\boldsymbol{s}}$. If $\boldsymbol{d}$ is some point on the plane, and $\boldsymbol{r}^{\boldsymbol{X}}$ is a 3D vector in absolute space that points to any point on the plane, then the equation for all points that would lay on this pattern plane is shown by Equation 19.

$$\hat{\boldsymbol{n}} \cdot \boldsymbol{r}^{\boldsymbol{X}} = \hat{\boldsymbol{n}} \cdot \boldsymbol{d} \qquad 19$$

For reasons important later, the arbitrary point $\boldsymbol{d}$ is chosen to be the plane's origin point. To perform the reverse projection from a point on this plane to the image plane, simultaneous equations of projection and the pattern plane equation needs to be solved. From this, the 3D location of the point on a pattern plane that corresponds to an image location can be determined through simple matrix transformation. And from that, we can get the *r*-*s* location on the pattern plane.

Forward projection using homogenous transformations is done as follows, where $\boldsymbol{x}^{\boldsymbol{H}}$ becomes a 2D homogenous vector where the 3rd entry represents the scale of the vector. This is shown by Equation 20.

$$\begin{bmatrix} f\boldsymbol{I}_{2\times 2} & \boldsymbol{0}_{2\times 1} \\ \boldsymbol{0}_{1\times 2} & 1 \end{bmatrix} \boldsymbol{r}^{\boldsymbol{X}} = \boldsymbol{x}^{\boldsymbol{H}} \qquad 20$$

The $\boldsymbol{x}$ vector can be calculated from the $\boldsymbol{x}^{\boldsymbol{H}}$ by simply dividing the first two elements by its third element, as shown by Equation 21.

$$\boldsymbol{x} = \frac{1}{x^H{}_z} \begin{pmatrix} x^H{}_x \\ x^H{}_y \end{pmatrix} \qquad 21$$

To now find $\boldsymbol{r}^{\boldsymbol{X}}$ from $\boldsymbol{x}$ we need to perform the reverse of this transformation. To do so, it is easier to frame this process as a simple set of three simultaneous equations without using homogenous vectors. First, a substitution of Equation 21 into Equation 20 is done, noting that $x^H{}_z$ is merely equal to $r^X{}_z$. This substitution is shown by Equation 22. The aim of this is to remove any mention of $\boldsymbol{r}^{\boldsymbol{X}}$ in the-right hand side.

$$\begin{bmatrix} f\boldsymbol{I}_{2\times 2} & \boldsymbol{0}_{2\times 1} \\ \boldsymbol{0}_{1\times 2} & 1 \end{bmatrix} \boldsymbol{r}^{\boldsymbol{X}} = \begin{pmatrix} \boldsymbol{x} r^X{}_z \\ r^X{}_z \end{pmatrix} \qquad 22$$

With rearranging, this becomes Equation 23.

$$\begin{bmatrix} f\boldsymbol{I}_{2\times 2} & -\boldsymbol{x} \\ \boldsymbol{0}_{1\times 2} & 1 \end{bmatrix} \boldsymbol{r}^{\boldsymbol{X}} = \begin{pmatrix} \boldsymbol{0}_{2\times 1} \\ r^X{}_z \end{pmatrix} \qquad 23$$

However, there is still an $r^X{}_z$ term left on the right-hand side. And this cannot be removed without under-defining the simultaneous equations, as $r^X{}_z$ is a free variable in this simultaneous equation alone. To solve this, we can use the fact that we know what $r^X{}_z$ is given we have a definition of the pattern plane from Equation 19. One could try and solve for $r^X{}_z$ directly and substitute, but this would be tedious and wouldn't remove mention of $\boldsymbol{r}^{\boldsymbol{X}}$ and its terms from the right-hand side without more rearranging. Instead, we should notice that Equation 19 already has $\boldsymbol{r}^{\boldsymbol{X}}$ separated onto the left-hand side, and so can be substituted directly, as shown by Equation 24.

$$\begin{bmatrix} f\boldsymbol{I}_{2\times2} & -\boldsymbol{x} \\ \hat{\boldsymbol{n}}^{\mathrm{T}} & \end{bmatrix} \boldsymbol{r}^{\boldsymbol{X}} = \begin{pmatrix} \boldsymbol{0}_{2\times1} \\ \hat{\boldsymbol{n}} \cdot \boldsymbol{d} \end{pmatrix} \tag{24}$$

This adds a solution for $r^X{}_z$, making it no longer a free variable, and making the set of simultaneous equations solvable. From now on, this equation will be referred to in the form shown by Equation 25. Noting that χ is a function of $\boldsymbol{x}$.

$$\chi(\boldsymbol{x})\boldsymbol{r}^{\boldsymbol{X}} = \boldsymbol{q} \tag{25}$$

Now $\boldsymbol{r}^{\boldsymbol{X}}$ can be simply determined by inverting χ and multiplying it by $\boldsymbol{q}$. However, we want to find the 2D vector $\boldsymbol{r}$, the coordinates on the pattern plane. To do this we can again use the definition of the pattern plane in Equation 26 to determine the local $\boldsymbol{r}$ coordinates on the plane from the global $\boldsymbol{r}^{\boldsymbol{X}}$ coordinates by first defining the orthogonal matrix $\boldsymbol{Q}$.

$$\boldsymbol{Q} = [\hat{\boldsymbol{r}} \quad \hat{\boldsymbol{s}}] \tag{26}$$

This represents the transformation of the local pattern plane coordinates to global coordinates. Now the full transformation of points represented in the pattern's local frame to the global camera frame can be calculated using Equation 27, where $\boldsymbol{d}$ is defined as the origin of the pattern.

$$\boldsymbol{Qr} + \boldsymbol{d} = \boldsymbol{r}^{\boldsymbol{X}} \tag{27}$$

Therefore, combining Equation 25 and Equation 27, we can determine $\boldsymbol{r}(\boldsymbol{x})$ as shown by Equation 28.

$$\boldsymbol{r}(\boldsymbol{x}) = \boldsymbol{Q}^{\mathrm{T}}(\chi^{-1}(\boldsymbol{x})\boldsymbol{q} - \boldsymbol{d}) \tag{28}$$

Note that $\chi^{-1}(\boldsymbol{x})\boldsymbol{q}$ can be simplified in form by defining the vector $\boldsymbol{x}^{\boldsymbol{X}}$, a vector in global coordinates which represent points on the camera's image plane centred at $+f$ on the z-axis, shown by Equation 29.

$$\boldsymbol{x}^{\boldsymbol{X}} = \begin{pmatrix} x \\ y \\ f \end{pmatrix} \tag{29}$$

Hence, the expanded form is shown in Equation 30, where $\hat{\boldsymbol{n}} = [a\ b\ c]^{\mathrm{T}}$.

$$\chi^{-\mathbf{1}}\boldsymbol{q} = \frac{1}{\hat{\boldsymbol{n}} \cdot \boldsymbol{x}^{\boldsymbol{X}}} \begin{bmatrix} (f\boldsymbol{x}[a \quad b])^{-1} + c\boldsymbol{I}_{2\times2} & \boldsymbol{x}^{\boldsymbol{X}} \\ -[a \quad b] & \end{bmatrix} \begin{pmatrix} \boldsymbol{0}_{2\times1} \\ \hat{\boldsymbol{n}} \cdot \boldsymbol{d} \end{pmatrix} = \frac{\hat{\boldsymbol{n}} \cdot \boldsymbol{d}}{\hat{\boldsymbol{n}} \cdot \boldsymbol{x}^{\boldsymbol{X}}} \boldsymbol{x}^{\boldsymbol{X}} \tag{30}$$

This makes the final simplified form of the coordinate reverse-projection as shown by Equation 31.

$$\boldsymbol{r}(\boldsymbol{x}) = \frac{\hat{\boldsymbol{n}} \cdot \boldsymbol{d}}{\hat{\boldsymbol{n}} \cdot \boldsymbol{x}^{\boldsymbol{X}}} \boldsymbol{Q}^{\mathrm{T}} \boldsymbol{x}^{\boldsymbol{X}} - \boldsymbol{Q}^{\mathrm{T}} \boldsymbol{d} \tag{31}$$

Notice that the $\hat{\mathbf{n}} \cdot \mathbf{d} \,/\, \hat{\mathbf{n}} \cdot \mathbf{x}^{\mathrm{X}}$ term merely represents projection along the normal if $\hat{\mathbf{n}} \cdot \mathbf{x}^{\mathrm{X}}$ was the focal length of the camera. This turns out to be equivalent to camera projection of that point at a distance along the optical axis.

In general, for multiple patterns, a given pattern, i, would be defined by Equation 32.

$$\boldsymbol{r}_{\mathrm{i}}(\boldsymbol{x}) = \frac{\hat{\boldsymbol{n}}_i \cdot \boldsymbol{d}_i}{\hat{\boldsymbol{n}}_i \cdot \boldsymbol{x}^X} \boldsymbol{Q}_i{}^{\mathrm{T}} \boldsymbol{x}^X - \boldsymbol{Q}_i{}^{\mathrm{T}} \boldsymbol{d}_i \tag{32}$$

3.2.2. Applying the Fourier Theory

If we use Equation 32 to get the functions for the coordinate reverse-projection for two (or more) patterns, the Fourier theory can be applied to model the moiré pattern. Most generally, this boils down to the Equation 33 (to calculate the moiré frequency), the equation of the pattern phase as a function of its x-y image position, for a (k_1, k_2, …, k_n)-moiré with n patterns.

$$\boldsymbol{\phi}_{\boldsymbol{m}}(\boldsymbol{x}) = k_1 \boldsymbol{f}_{\boldsymbol{1}} \cdot \boldsymbol{r}_{\boldsymbol{1}}(\boldsymbol{x}) + k_2 \boldsymbol{f}_{\boldsymbol{2}} \cdot \boldsymbol{r}_{\boldsymbol{2}}(\boldsymbol{x}) + \cdots + k_n \boldsymbol{f}_{\boldsymbol{n}} \cdot \boldsymbol{r}_{\boldsymbol{n}}(\boldsymbol{x}) \tag{33}$$

Or, more compactly, we get Equation 34.

$$\boldsymbol{\phi}_{\boldsymbol{m}}(\boldsymbol{x}) = \boldsymbol{F}\boldsymbol{K}\boldsymbol{R}^{\mathrm{T}} \tag{34}$$

With the following definitions:

$$\boldsymbol{F} = [\boldsymbol{f}_1 \quad \dots \quad \boldsymbol{f}_{\boldsymbol{n}}]$$

$$\boldsymbol{R} = [\boldsymbol{r}_1(\boldsymbol{x}) \quad \dots \quad \boldsymbol{r}_{\boldsymbol{n}}(\boldsymbol{x})]$$

$$\boldsymbol{K} = \begin{bmatrix} k_1 & \dots & 0 \\ \vdots & \ddots & \vdots \\ 0 & \dots & k_n \end{bmatrix}$$

Substitute this into the transmittance function from Equation 6 and we get the general model for the function of a moiré pattern generated from an arbitrary number of planar grating (sinusoidal) patterns in space, as shown by Equation 35.

$$P_m(\boldsymbol{x}) = \frac{1}{2}\left(1 + \cos\left(2\pi \boldsymbol{\phi}_{\boldsymbol{m}}(\boldsymbol{x})\right)\right) \tag{35}$$

3.2.3. Applied Two-Pattern Model

For the case of a (1, −1)-moiré generated from only two patterns, we get Equation 36 from Equation 33.

$$\boldsymbol{\phi}_{\boldsymbol{m}}(\boldsymbol{x}) = \boldsymbol{f}_{\boldsymbol{1}} \cdot \boldsymbol{r}_{\boldsymbol{1}}(\boldsymbol{x}) - \boldsymbol{f}_{\boldsymbol{2}} \cdot \boldsymbol{r}_{\boldsymbol{2}}(\boldsymbol{x}) \tag{36}$$

This is the analogous to the moiré frequency as a function of $\boldsymbol{x}$ from Equation 16. However, more accurately, this term also incorporates the phase term ($\boldsymbol{f_d} \cdot \boldsymbol{\Delta X}$). That is, it is the phase offset of the sinusoidal function representing the moiré pattern at a given x-y position in the camera image.

If both patterns of the moiré pattern are co-planar, that is they are parallel, then this equation can be expanded and simplified into Equation 37.

$$\boldsymbol{\phi}_{\boldsymbol{m}} = \frac{\boldsymbol{f}_{\boldsymbol{1}}}{D} \cdot \boldsymbol{Q}^{\mathrm{T}} \left(\frac{\boldsymbol{x}^X}{\hat{\boldsymbol{n}} \cdot \boldsymbol{x}^X} \left((D-1)\hat{\boldsymbol{n}} \cdot \boldsymbol{d}_{\boldsymbol{1}} - d \right) - (D-1)\boldsymbol{d}_{\boldsymbol{1}} \right) \tag{37}$$

Where $\boldsymbol{q_d} = [0, 0, d]^{\mathrm{T}}$, D = f_1/f_2, and $d_2 = d_1 + d$. Also note that $\boldsymbol{Q_1} = \boldsymbol{Q_2} = \boldsymbol{Q}$ and therefore $\hat{\boldsymbol{n}}_{\boldsymbol{1}} = \hat{\boldsymbol{n}}_{\boldsymbol{2}} = \hat{\boldsymbol{n}}$, since the patterns are co-planar.

Further assumptions based on the setup can be made to further simplify the model. This can turn certain situations to have purely analytic solutions for certain moiré setups, given you can measure the information from the view of the moiré pattern. The initial simpler formula in Section 3.1 can be derived as special cases of this more general model.

3.3. MATLAB Simulation

A MATLAB simulation was developed that did both analytic simulation as well as a numeric simulation for comparison. This was an OOP-Based implementation which allows to easily make different types of moiré patterns and utilise the more general model defined above. This model makes no extra assumptions about the number of patterns, but only moiré patterns made of two patterns were investigated using it. The MATLAB simulation consists of a CGrating class to model individual grating patterns, a CMoiréPattern which consists of multiple CGratings to make a moiré pattern, and a CPinholeCamera class to model the pinhole camera. A CMoireSim class then takes a CMoirePattern and a CPinholeCamera and uses them to simulate a moiré pattern, being able to generate camera images of the moiré pattern. A simple overview of the simulation architecture is shown by Figure 15. CPose is just a class that contains a homogenous matrix representing pose information that provides useful methods for dealing with homogenous transformations. The "params" property of the CPinholeCamera stores information about camera parameters, such as its vertical and horizontal resolution. The function R(…) from the CGrating is the $\boldsymbol{r_i}$ (for the ith pattern) from Equation 33. And the property K for CMoire is the vector of the k interference modes of each of the k patterns given to it. The model(…) function for each of the classes with a model function will return the $n \times m$ image of the moiré pattern, according to the image resolution.

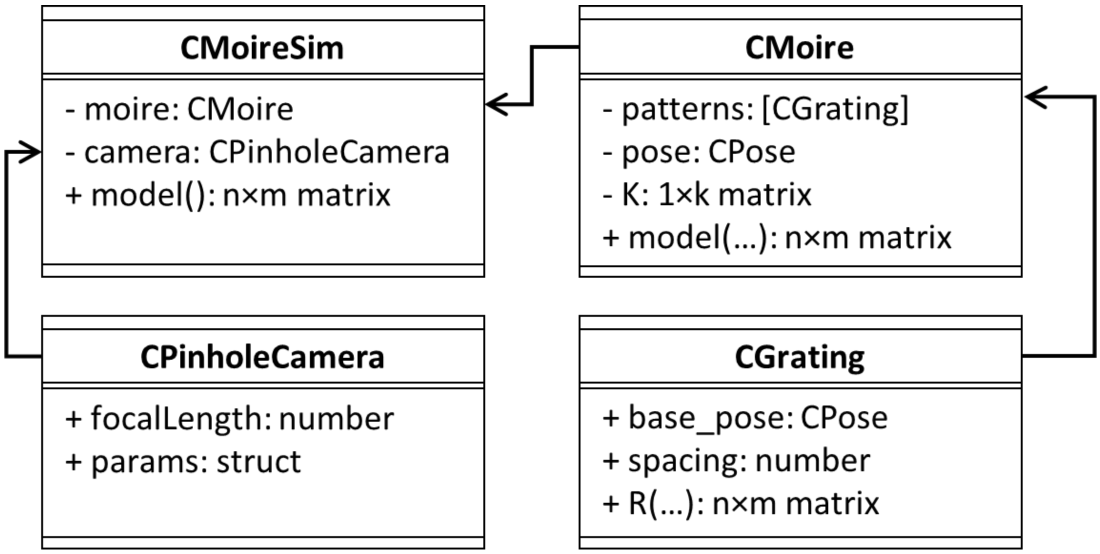

Figure 15: Overview of simulator architecture.

This simulation first takes poses of where two (or more) patterns were in space, as well as the size (height and width) of these patterns. The only available type of patterns in the simulation are grating patterns, so their spacing (and therefore frequency) is also given. These poses determined where the patterns are positions locally in the moiré pattern space.

A pose for where the moiré pattern is positioned in global space is given to place the moiré pattern in space. The camera is also assumed to be at the origin pointing in the *z*-direction. Making the *z*-axis the optical axis of the camera, +*y* as down the camera image, and +*x* as across the image from left to right. The focal length and resolution of this camera are needed for the camera simulator. Figure 16 shows an example of a moiré pattern visualised in space using the CMoire class. The red, green, and blue lines are the *x*-, *y*-, and *z*-axis of the moiré pattern. This shows the two grating patterns that make up the moiré pattern in space. The XYZ axes are the global camera frame, where the camera is centred at the origin (not depicted) pointing along its optical (Z) axis. This visualisation can also be generated as a wireframe if the detailed grating patterns are too dense and cause a slowdown in the simulation or impair the visualisation.

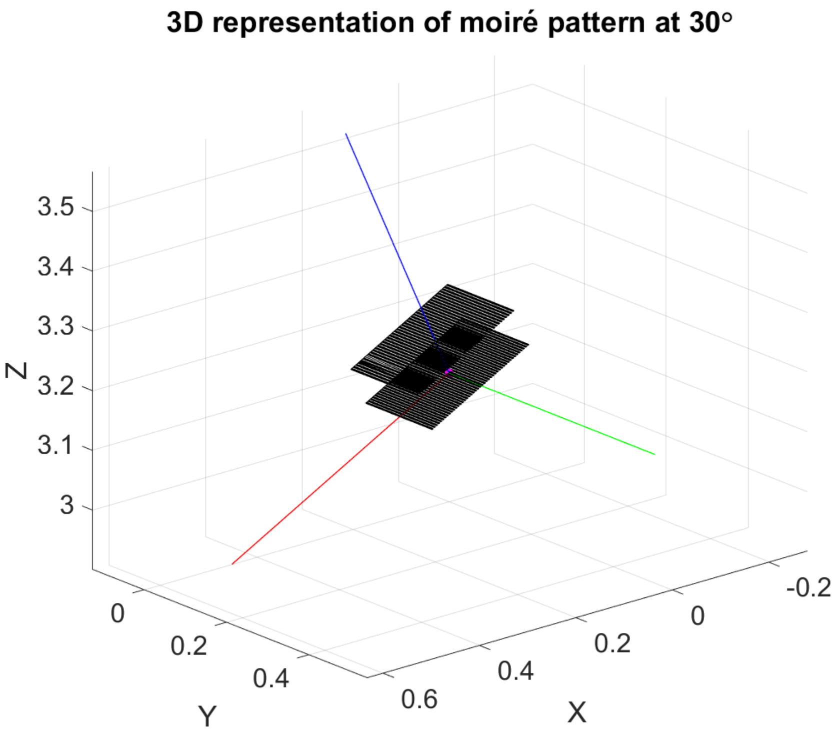

Figure 16: Simulated moiré pattern visualisation with axes generated by the CMoire class.

The moiré pattern and the camera are then passed to a CMoireSim which then takes this information and applies the theory developed in Section 3.2 to be used to generate modelled images of the moiré pattern, taking into account the size of the moiré pattern (so only that portion is visible). The CMoireSim can generate analytic and numeric representations of the moiré pattern. The analytic method is used to generate a greyscale image. The numeric method exists mostly for visualisation and performs camera projection of all of the 3D points of the moiré pattern's visualisation geometry shown in Figure 16. Figure 17 shows an example of the simulator generating these moiré pattern images, comparing them to a real-world example moiré of the same setup at a $-10°$ angle about the y-axis. This image is one of the images from the data gathered during testing. These images are cropped in on just the moiré pattern.

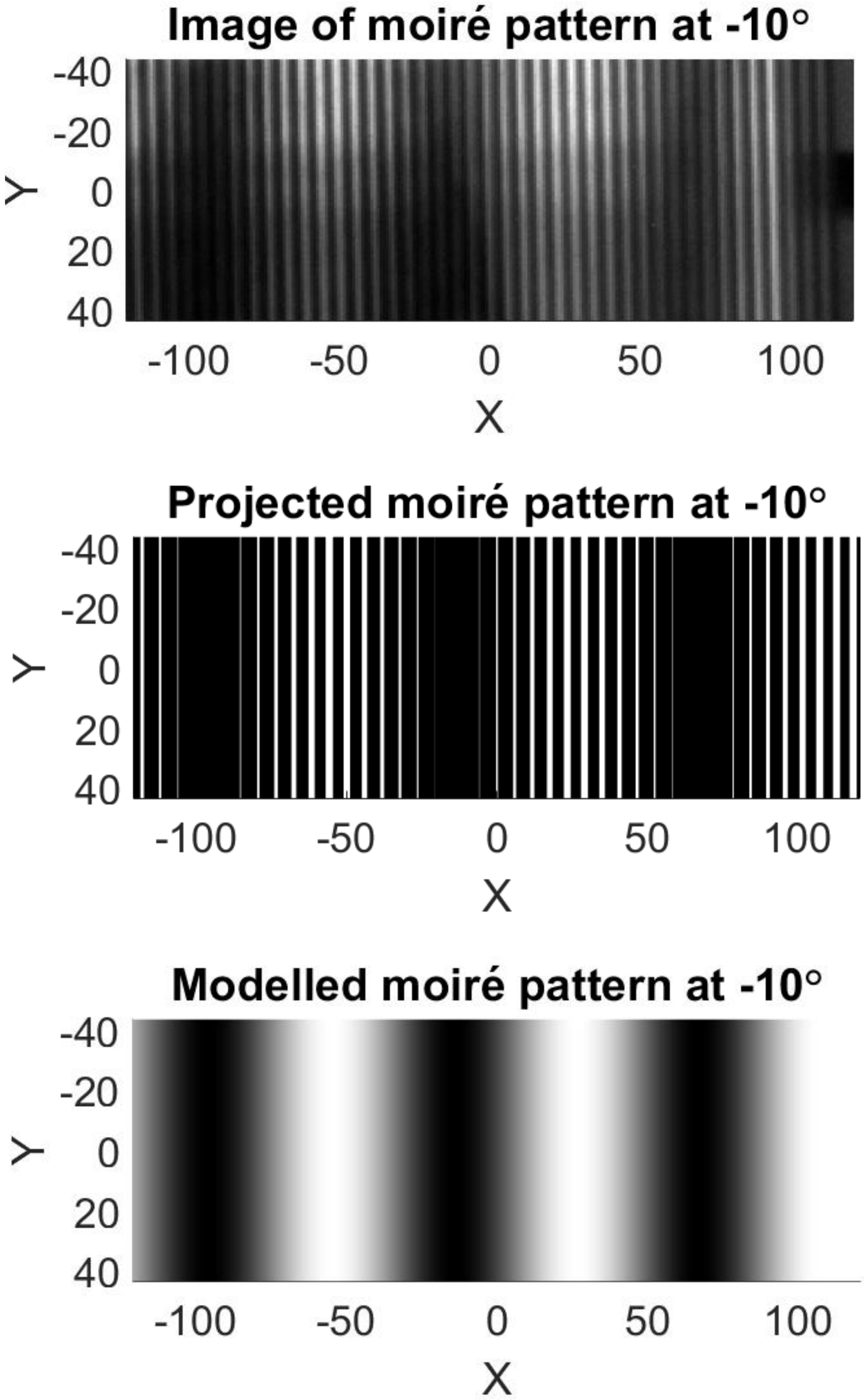

Figure 17: Comparison of true image of moiré against the numeric projection and analytic model simulations.

A CSolver class takes a CMoireSim and an observation of a camera image, which can either be a real or simulated image of the right dimensions, and tries to determine the parameters of the moiré pattern. The parameters can be set in advanced and, in this thesis, the solver is tested in only determining the y-tilt angle of a pattern from its image. The solver uses the Levenberg–

Marquardt optimisation algorithm implemented by a 3rd party library called "levmar" to solve for the parameters [42].

A class for Monte Carlo sensitivity analysis was developed to process the data for the more vigorous angle experiments performed later. This class, CMoireMonteCarlo, takes in a CSolver and its associated CMoireSim and runs trials on a set of input data. This input data consists of images of a moiré pattern at various tilt angles. It then runs the solver for each data point and saves the results to be analysed later for determining the accuracy of the angle estimates of the solver at each angle. Following is a more detailed technical explanation of the object-oriented design of the MATLAB simulator.

3.3.1. CGrating

The CGrating class represents one pattern to be a part of a whole moiré pattern. This pattern is a grating pattern as of the kind shown in Figure 11. This keeps track of all the geometry of a pattern's grating pattern for numeric simulation as well as the data about the geometry, such as its spacing and pose. This class also takes the local base pose of where the grating is in the patterns local frame, as well as its calculated absolute pose. The pattern can be moved using its "move" method. The class also provides methods for calculating its projection for a given camera as described by Equation 34 which can be used by the moiré class for performing the analytic model. It also contains the important R(…) function used to generate the moiré model for the later classes. This function takes three inputs: a vector of *x* values, a vector of *y* values, and the focal length of a camera. It performs the "reverse projection" in 3D space and returns where each of the *x*-*y* pairs map from the image plane to the *r*-*s* space on the pattern plane. This is used by the model function of the CMoire class to calculate how the grating's function (a sinusoid) maps onto the image plane when calculating the moiré interference.

3.3.2. CMoirePattern

The CMoirePattern class takes in any number of created CGrating classes as well as the global pose of the moiré pattern in space. The pattern can be moved or rotated using its own "move" method. The moiré pattern can be projected onto a 2D plane given a camera, either numerically or analytically using the model. These methods call to each of the methods of the CGrating classes and combined them according to the model in Equation 33.

3.3.3. CPinholeCamera

A pinhole camera model is the chosen camera model for this project. Hence, the CPinholeCamera class merely implements this camera projection model. The pinhole camera model merely scales the size of points in space based on their distance from a camera along its optical axis (the *z*-axis) centred at the origin. This is used purely for the numeric model, typically used for visualisation. The CPinholeCamera model is also useful having the information about the camera such as its focal length and horizontal and vertical resolution stored in its "params" property.

3.3.4. CMoireSim

The CMoireSim class takes and manages a CMoirePattern object and a CPinholeCamera model. It serves as a wrapper for these objects, creating an abstracted interface with the CMoireSim class performing all camera projection based on the parameters of the CPinholeCamera. It also allows methods to "vectorise" and "devectorise" itself such that the entire CMoirePattern–CPinholeCamera system kept by the CMoireSim can be represented as a set of parameters. This is important for the optimisation algorithm as these are the parameters it can optimise for.

3.3.5. CSolver

The CSolver class is the class that takes a CMoireSim with some configuration and is then uses it to attempt to determine certain parameters of a moiré pattern from given images. The CSolver is given a CMoireSim class as well as configuration options for things such as the type of optimisation algorithm to use, the maximum iterations, and a Boolean vector indicating which CMoireSim parameters to care about. This vector tells the CSolver which parameters to adjust and solver for. In the experiments conducted, only the *y*-rotation (tilt) of the moiré pattern was of interest, so only the vector element corresponding to this parameter was set to true. The CSolver then has a "solve" method which takes an initial guess for this parameter as well as the image observation. This image should match the size and resolution of the image the CMoireSim will generate when using its analytic model. The CSolver then attempts to determine the original parameter(s) of the moiré pattern for that the image was taken of. To do this the solver uses a third-party implementation of the Levenberg–Marquardt optimisation algorithm. The solver takes the 2D correlation between the real image and a moiré simulator's generated image and attempts to find the parameters, or tilt angle, that gets this value as close 1 as possible. This 2D correlation is calculated using MATLAB's "corr2" function. Hence the objective function, λ, for the algorithm is as shown by Equation 38.

$$\lambda(\boldsymbol{\theta}) = 1 - \mathrm{corr2}(\boldsymbol{Image}, \boldsymbol{ModelImage}(\boldsymbol{\theta})) \tag{38}$$

Where $\boldsymbol{\theta}$ is the vector of all parameters that are being optimised. In this case, this is a single-element vector containing only the *y*-rotation (tilt) angle. ***Image*** is a matrix of all the greyscale image points captured by a camera, and ***ModelImage*** is the method "model" implemented by the CMoireSim which returns a simulated image using the model given a set of parameters $\boldsymbol{\theta}$.

3.3.6. CMoireMonteCarlo

The CMoireMonteCarlo class takes a CSolver as well as its corresponding CMoireSim and performs a Monte Carlo sensitivity analysis on the CSolver from a list of image files. The files need to have a consistent naming convention. The Monte Carlo analysis then runs the CSolver on each image for several different initial guesses and saves the results of the optimised parameters to a file for data analysis. This data is then compared against the true values of the original moiré pattern. In the experiments performed, the CSolver is only trying to determine the *y*-rotation (tilt) of the moiré pattern. So, each of the determined values for the tilt is saved for each image with each initial guess. This is then compared against the measured value for the moiré tilt to determine the accuracy of the moiré simulation, its model, and the solver.

3.4. Other Investigated Patterns

This section serves to overview a few pattern ideas that were explored in the process of designing which patterns would be used for experiments. One of these pattern types can be modelled by the theory developed and MATLAB framework created. So, this section also serves to demonstrate some of the other types of patterns this model can simulate.

One such pattern investigated early on was the idea of a moiré pattern where two generating grating patterns were angled relative to one another, as shown by Figure 18. The reason this pattern type showed interest is because when the patterns are angled like this, the moiré pattern generated seems to curve and point to the middle of the pattern. That is, when this centre pattern of this fringe is perfectly in the middle of the pattern, it means that the pattern is perfectly in line with the camera's image plane, with no rotation or horizontal offset.

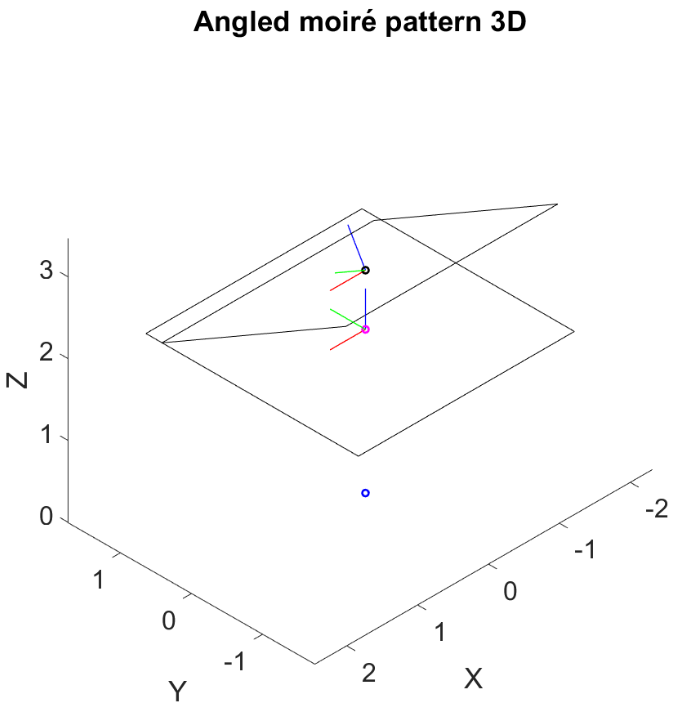

Figure 18: A wireframe example of an angled moiré pattern. The lowest blue circle is the position of the camera.

Figure 19 shows the fringe behaviour of this type of pattern as generated by the numeric MATLAB model. A parabolic pattern emerges where the *y*-asymptote is always the vertical *y*-axis at *x* equals 0 in the image plane as long as the camera and pattern are parallel. This does not change even as the pattern moves laterally. The *x*-asymptote, on the other hand, will move as the pattern moves up and down. This kind of pattern could lend itself use in aligning something directly with a marker. Once the *y*-asymptote fringe is aligned directly in the centre of the moiré pattern, then that means the camera is directly in line with it. Comparing Figure

19 to Figure 20 also shows that the MATLAB model is capable of capturing this phenomenon using its analytical model described in Section 3.2.

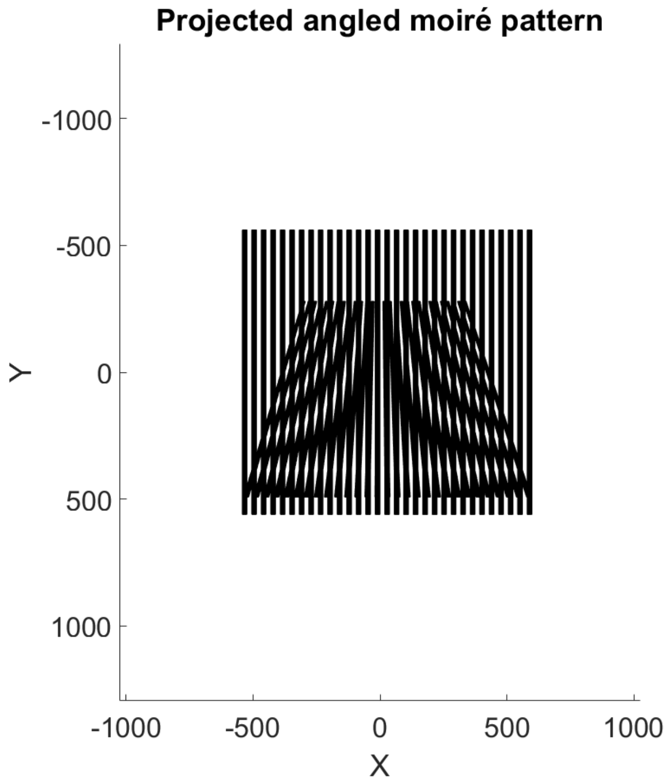

Figure 19: Numeric simulation of the projection of an angled moiré pattern.

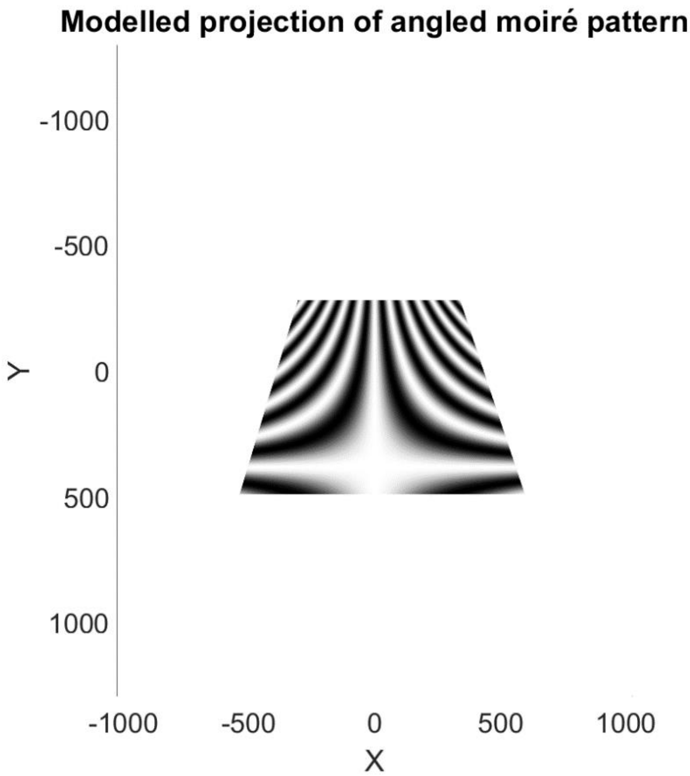

Figure 20: Analytically modelled representation of the angled moiré projection.

Some other concepts were also discussed but not significantly investigated or modelled. Such as the idea of curved or cylindrical patterns. Depending on the orientation of the gratings, these patterns have different sorts of interesting observed properties. If the pattern is wrapped horizontally, such as in Figure 21, then the moiré pattern has a similar “fixed 0-axis” behaviour as the angled pattern, except the cylindrical patterns are not affected by being viewed from different angles as they are rotationally symmetric. As seen in Figure 21, there is a line in the middle of the image that all other fringes curve away from. This is always centred vertically in the middle of the camera’s image so long as the camera is parallel to the closest side of the pattern.

Figure 21: Cylindrical moiré pattern with grating wrapped horizontally.

The behaviour of this type of moiré pattern idea shows promise for specific positioning applications such as centring or aligning a camera to be parallel to a plane or even use in determining the tilt angle of the camera in one direction

When the grating pattern is wrapped vertically, like in Figure 22, you get fringes a lot like you would with a regular moiré pattern. However these fringes widen near the edges of the moiré pattern and, as with the other cylindrical pattern, these fringes do not change based on viewing angle. They only change phase as the viewer moves.

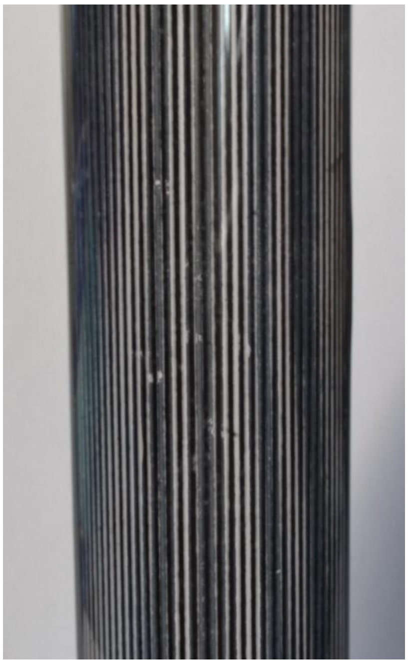

Figure 22: Cylindrical moiré pattern with grating wrapped vertically.

This could potentially give a reliable and consistent way to determine camera position along an axis from any angle, as long as this phase is tracked. This differs from the previous example as you may not always be able to see the centre fringe of the horizontally aligned cylindrical pattern. Whereas for this pattern this would not be an issue.

3.5. Tests

3.5.1. First Tests

Some preliminary experiments were run to test if the basic model was accurate before it was further developed. This was done in two separates tests. A lateral translation test and a distance test. A moiré pattern was set up by placing two grating patterns on stands in front of one another, as shown by Figure 23. The gratings' distance apart was measured and, for the distance test, the front grating was rotated relative to the other, about the same axis as the camera's optical axis, and this angle was measured. For the distance tests, several photographs were taken at distances ranging from 0.1 m to 2.3 m. For the lateral translations test, the phone was mounted to a heavy laterally sliding apparatus to keep it still and align it parallel to the moiré pattern. Both tests used patterns with spacings of 2 mm and 2.1 mm for pattern 1 and pattern 2 respectively.

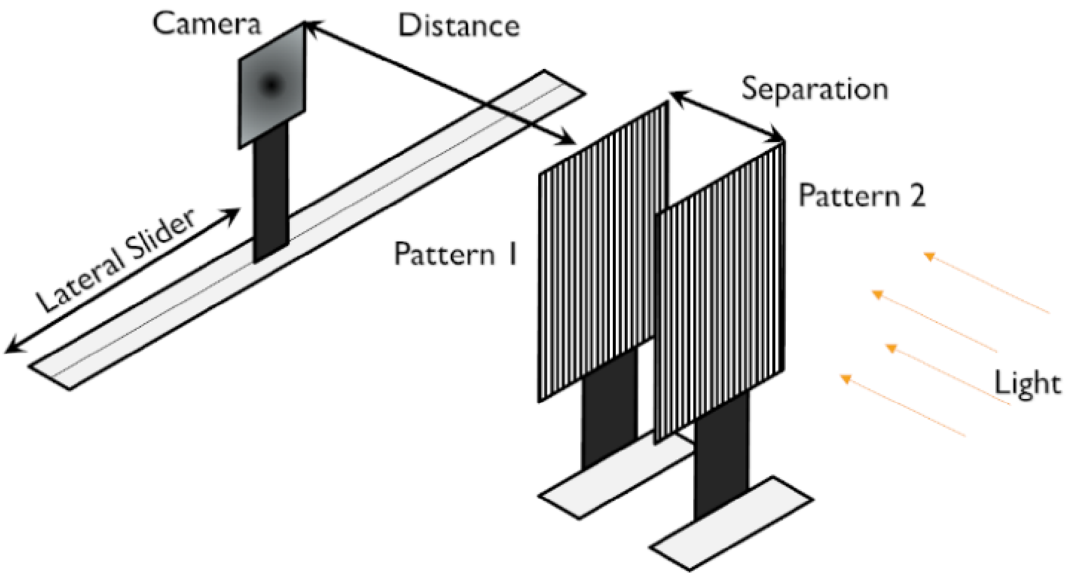

Figure 23: Experimental setup for first tests showing important parameters for the test.

Several photographs were then taken at different positions along this slider, noting how far along the slider they had been moved from its starting position. A 12 MP, f/2.2, 1.25µm pixel size phone camera was used to capture the images. After the fact, the position for which the moiré pattern had a bright fringe directly down the centre of a camera image was taken as the "0" point, and all other positions on the slider were recalculated relative to this point.

In the actual experimental setup, pattern 2 is affixed to the light source to shine the light through both patterns. Figure 24 shows a photograph of the actual setup used taken from the lateral translation dataset.

Figure 24: Photograph of the setup used for the first tests.

An interesting phenomenon occurs when you rotate the front-most pattern (pattern 1) slightly (about the same axis as the camera's optical axis). This causes the pattern to shift as the camera view moves closer and further to it. This is the basis of how the distance experiments work. As described and predicted by Equation 13, the shifting seen is that the moiré pattern appears to rotate clockwise in the plane as the view gets further or closer. This is assuming that the spacing of pattern 1 is smaller than that of pattern 2 and that the rotational offset of pattern 1 is anti-clockwise and not too large (otherwise the moiré interference pattern is not prominent). This is demonstrated by Figure 25 and Figure 26, where the moiré pattern slowly rotates asymptotically to the vertical the further away the camera is from it. Here, this is the setup used for the distance experiments, and pattern 1 has been rotated counter-clockwise by 7°.

Figure 25: Moiré pattern distance experiment setup at roughly 0.7 meters.

Figure 26: Moiré pattern distance experiment setup at roughly 1.2 meters.

What is interesting to note is that this moiré pattern behaviour will never rotate further than 90° from the horizontal, or positive *x*-axis (it will asymptotically approach the vertical). This is true both ways, as the moiré pattern will never rotate further than −90° from the positive *x*-axis as the camera slowly approaches zero. This causes the angle sensitivity of distances closest to zero to be the most sensitive, becoming less sensitive as the camera gets further away. However, one thing that can be done is that the moiré pattern can be designed such that the distance at which the moiré pattern is perfectly vertical is predetermined. This means that decisions can be made on the working range of the distance as the angles between –90° and 0° to the *x*-axis will be the most sensitive. This distance at which the moiré pattern is horizontal can be easily designed using either Equation 13 or Equation 14. In which case either equation should be rearranged in terms of D, d, or θ_1. Two of these parameters will need to be decided by other means or constraints (such as not having a separation, d, larger than a certain distance), then the third can be calculated. D is typically calculated via its definition, f_1/f_2. For these distance tests, the distance at which the fringe is horizontal was designed to be about 1 m and was roughly 980 mm in practice. For the turntable tests this method was also used for designing the patterns and the exact calculations on how to do this will be discussed in that section.

3.5.2. Turntable Tests

Several tests were run to test the accuracy of the generalised model and the moiré estimation method. Two Perspex panels with grating panels affixed to the side were attached to a precise turn-table apparatus. This turntable could position itself accurately within 1 arcsecond of accuracy on two rotational axes. One pattern was an opaque printed grating pattern and the other was a transparent grating pattern. The opaque pattern, pattern 2, had a spacing of 5.5 mm and was placed at the back; and the transparent pattern, pattern 1, had a spacing of 5 mm and was placed at the front. These distances were calculated using the theory so that approximately three to four fringes would always be visible on the moiré pattern given the chosen separation and camera distance the experiment was to be run at. These two patterns also needed to be aligned properly so that the edge of a fringe of both patterns were aligned with the centre of rotation of the turntable. A photograph of this setup is shown by Figure 27.

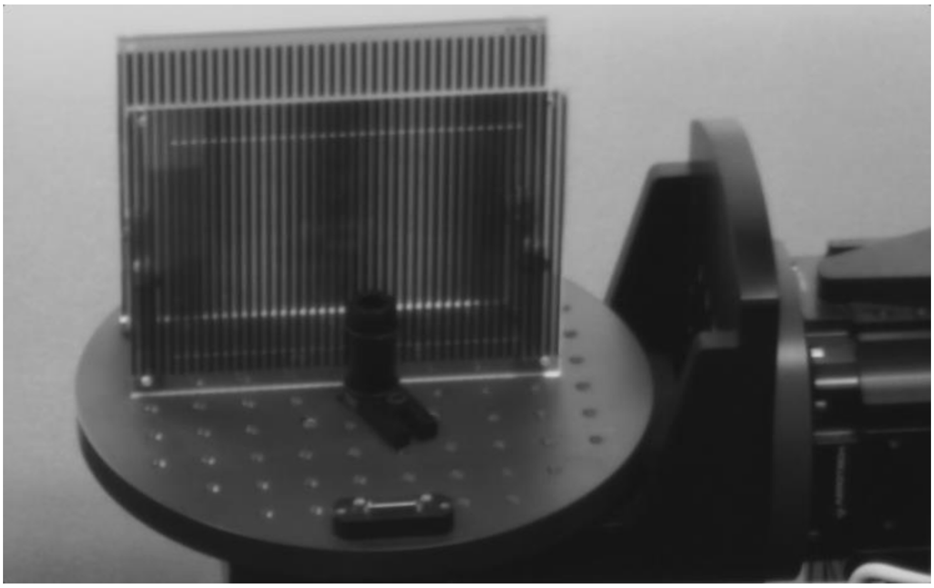

Figure 27: Photograph of the turntable experimental setup.

A camera was set up a distance away pointed parallel to the moiré pattern, and several images were taken with the pattern panned at varying angles to the camera. Figure 28 shows this full setup, detailing the measured and varied parameters in the experiment. In the figure, f is the focal length of the camera, d_{p1s} is the distance from the front of pattern 1 to the image sensor of the camera, d_{p1c} is the distance from the front of pattern 1 to the rotational centre of the turntable, d_{p1p2} is the inner distance between pattern 1 and pattern 2, and θ_{offset} is the angular offset between the optical axis of the camera and the turntable's resting 0° point. The rotational centre of the turntable is shown in green, with an indication of the y-tilt parameter, which is the varied parameter throughout the experiment.

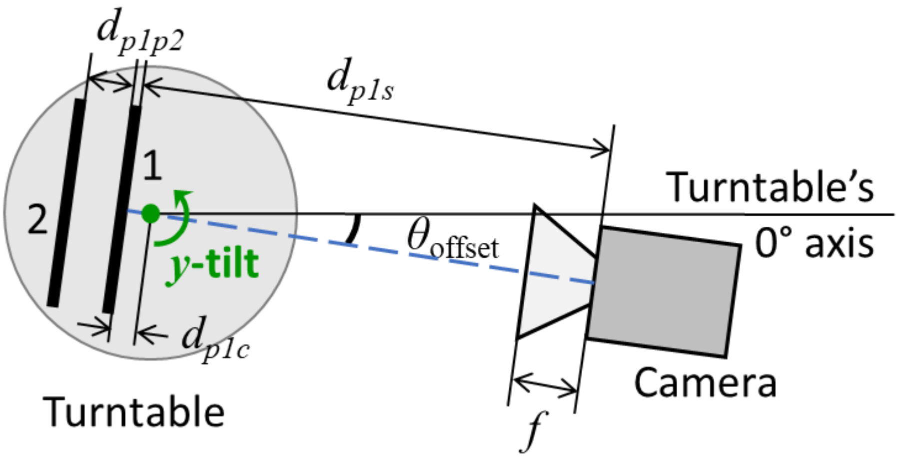

Figure 28: The setup for the turntable experiments detailing the measured parts of the setup. The black rectangles are pattern 1 and pattern 2, indicated by "1" and "2".

The Perspex panels consist of two Perspex plates with the grating patterns sandwiched between them. Therefore, the thicknesses of the inner-most Perspex plate of each Perspex panel also needed to be known. These are not noted in Figure 28 but are called t_{p1} and t_{p2} for the thickness of pattern 1 and pattern 2 respectively, shown by Figure 29.

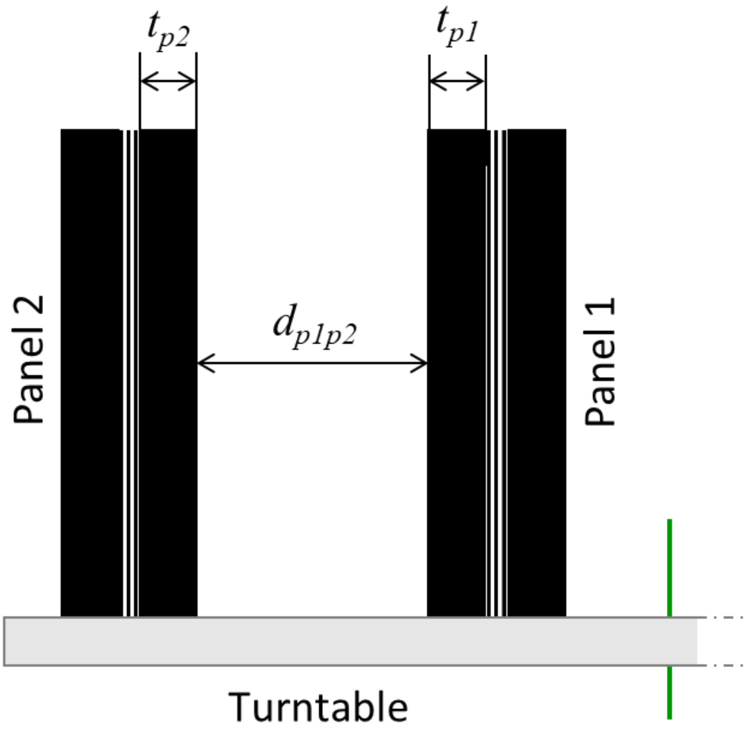

Figure 29: The thickness of the inner Perspex plate (shown in black) for each of the Perspex pattern panels.

Table 1 shows the measured values of each of these parameters. The focal length of the camera was merely taken from its specification.

Table 1: Measurements made of the turntable setup.

f [mm]	d_{p1s} [mm]	d_{p1c} [mm]	d_{p1p2} [mm]	t_{p1} [mm]	t_{p2} [mm]	θ_{offset} [°]
8	3125	1.38	63.35	3.80	3.79	5.05

Certain constant parameters required for the model were calculated from these measured parameters. The parameters required to be calculated were d_1, the distance from the camera's focal point to the centre of the moiré pattern (which is the centre of rotation for the turntable), and d, the distance between the grating patterns on the Perspex panels. These are calculated as shown by Equation 39 and Equation 42.

$$d_1 = d_{p1s} - f \quad 39$$

$$d = t_{p2} + d_{p1p2} + t_{p1} \quad 40$$

The final values of all fixed parameters important to the model are shown in Table 2, including the spacing values of pattern 1 and pattern 2, p_1 and p_2 respectively.

Table 2: Fixed parameters required by the simulator.

d_1 [mm]	d [mm]	p_1 [mm]	p_2 [mm]
3115.6	70.9	5	5.5

To design the patterns for this experiment, these parameters were determined by using the developed theory to design a pattern to be suited for the experimental setup. This was done by using the theory to determine an equation in terms of the free parameters of the experiment and deciding iteratively the vicinity of these parameters. It did not matter if the parameters were exactly where they were designed to be when creating the patterns if they were close. It only mattered that we knew what those parameters were accurately after the fact (by measuring them after the experiments were run). To choose these parameters, Equation 12 was used to create this dependant equation for the free variables that needed to be decided. These free variables where the spacing of pattern 1 and 2 (captured as the spacing of pattern 1, p_1, and the ratio of their spacings, $D = p_2/p_1$), the separation between them, d, the length of the pattern, l, and the number of desired fringes visible, n, at a given distance, d_1. The number of fringes is important for visibility and so that the solver has enough information. Given some decided distance d_1, then the number of fringes visible is calculated by Equation 41.

$$n = \frac{l f_m f}{d_1} \qquad 41$$

Where f_m is the absolute value of $\boldsymbol{f_m}$ as calculated by Equation 12. Since, in this example, the patterns are colinear (their gratings point in the same direction), then $\boldsymbol{f_m}$ only consists of an x component. Therefore, combining Equation 12 and Equation 41 gives Equation 42, a way to calculate D from all of the other dependant components. Noting that the focal length of the camera, f, cancels out and the camera parameters do not need to be known to design the moiré pattern.

$$D = \frac{\left(1 + \frac{d}{d_1}\right)}{\left(1 - \frac{p_1 n}{l}\right)} \qquad 42$$

It was decided that the pattern should show roughly 4 fringes, therefore $n = 4$, as this gives good visibility of at least 3 dark fringes for any angle for the solver. Pattern 1's spacing shouldn't be less than 5 mm, as too small of a spacing reduces contrast, but too large of a spacing reduces the moiré effect. Therefore 5 mm was chosen. The length of the pattern was roughly that of an A4 sheet of paper at l = 297 mm. And the spacing was decided to be roughly 50 mm. This was based on as large a spacing as could be feasibly tested in the turntable. The larger the spacing the more sensitive the moiré pattern is to rotation; hence this was changed later as the experiment was set up to be larger. Similarly, 3 m was chosen for d_1 as this was the furthest distance the camera could be placed away from the pattern in the setup, although the pattern was also expected to work for distances of 1 m to 10 m. With a value chosen for all the other parameters, D was calculated and used to calculate the spacing for pattern 2, p_2, using Equation 42. This gave a D of about 1.10, meaning that p_2 was calculated to be 5.5 mm.

After the experiments were run, all the required parameters were measured that were shown by Figure 28 and Figure 29. The distance between the camera's image plane/sensor and the front of the first pattern (d_{p1c}) was measured using a laser sight. The laser sight was also used to measure the angular offset of the turntable required for the pattern to be parallel to the camera. This was done by setting the laser on the turntable and aligning the laser point with the centre of the camera by rotating the turntable's y-tilt. This is important for matching the angles calculated via simulation with the real-world turntable angles. The distance between the two patterns (d_{p1p2}), the thicknesses of the Perspex these patterns were affixed to (t_{p1} and t_{p2}), and the distance the centre of pattern 1 was from the rotation centre of the turntable (d_{p1c}) were all measured using Vanier callipers.

Three experiments were run on the turntable. First with panning from −30° to 30° in steps of 1°, second −5° to 5° in steps of 0.5°, and third −1° to 1° in steps of 0.1°. This means the total pictures taken for each experiment were 61, 21, and 21 respectively. A Python script was written to process the sets of images recorded. This script was a simple command-line interface to rename all images in a set to the angle the turntable was set to when each image was taken. It then also cropped each of the images to a specified size, which was used to crop the image to only contain the pattern itself. This is so they were in a form ready for the MATLAB solver.

Once these images had been processed and cropped to the right scale, a MATLAB sensitivity analysis was performed using the CMoireMonteCarlo class. The simulator was calibrated with all the known measured parameters of the experimental setup which are passed to the solver and the Monte Carlo sensitivity analyser. This calibrated simulator, when passed the measured angles from the experiment, also serves as the base-line for the accuracy comparison to the estimated angles. This is important for determining the accuracy of the estimated angles. The Monte Carlo analysis was then run for the three different tilt angle ranges: −30° to 30, −5° to 5°, and −1° to 1°. During this Monte Carlo analysis, the solver is run 3 times for each given image with different initial guesses. These initial guesses are chosen to be roughly around the true solution. One guess to close to the solution and the two others are either side of this guess by the angle step amount.

Figure 30 shows a flow diagram of the Monte Carlo simulations that were run. For the test using angles of −30° to 30° with 1° steps, there was a set of 61 images. For the other two tests, there was only a set of 21 images. In the diagram, the solver was run for every combination of three initial guesses and the image set used for a given test, storing each result for later grouped by image used from the image set (groups of three for each initial guess used). This means the solver was run a total of 183 times for the test using angles of –30° to 30° in steps of 1°, and 63 times for the other two tests.

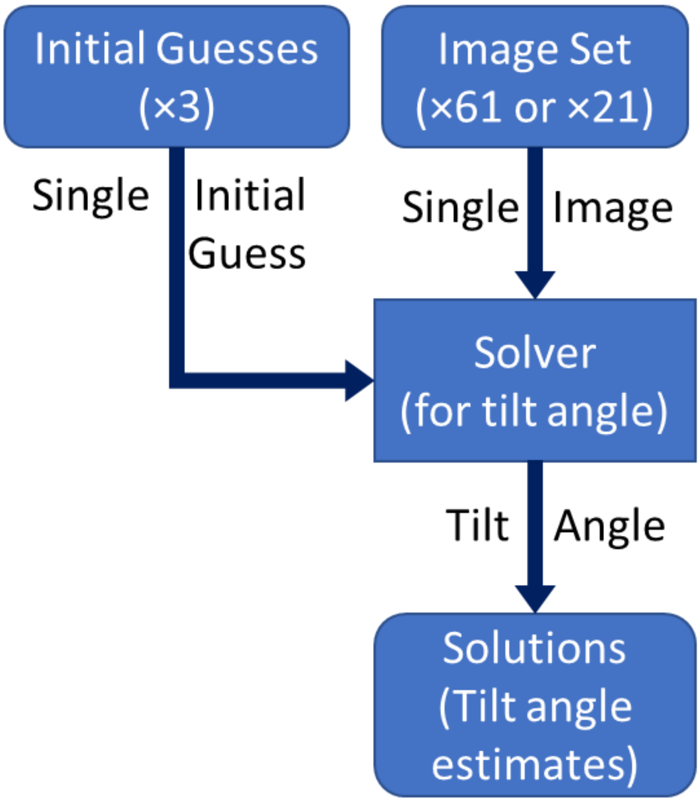

Figure 30: Monte Carlo simulations run.

The Monte Carlo simulations took about 3 hours to run. Once all Monte Carlo analyses had been run, the data gathered was compared against the true tilt values recorded by the turntable. This value is offset by the measured tilt angle offset to get the true tilt value expected relative to the camera's optical axis, which is how the model is represented. This data was then plotted and analysed.

4. RESULTS

4.1. First Tests

Table 3 shows the set parameters used for the camera lateral translation estimation experiments and their uncertainties. The *d* parameter is the distance between the patterns, d_1 is the distance to the first (closest) pattern. The p_1 parameter is the printed grating separation (inverse frequency) of pattern 1, and p_2 is the same for pattern 2.

Table 3: Set parameters for the camera lateral translation estimation experiments.

d [mm]	**d error [mm]**	**d_1 [mm]**	**d_1 error [mm]**	**p_1 [mm]**	**p_2 [mm]**
4	0.25	161	2	2	2.1

Figure 31 shows the plot of the recorded data and their error bars from the experiment performed to test the camera lateral translation estimation. The relative position given is the position relative to the measured position that was determined to be the zero-point. This was determined after the fact by finding the point that corresponds to when a fringe is centred directly down the centre of the camera image. This is necessary to match up with the assumptions of the theory. The spacing is the inverse of the moiré pattern frequency and is expected to be roughly the same between measurements. The raw data gathered to generate this graph can be found in Appendix A. The figure shows the behaviour of drifting down linearly before shooting back up close to the spacing value and drifting down again. However, due to under sampling this behaviour is not obvious and is broken from −100 to −30.

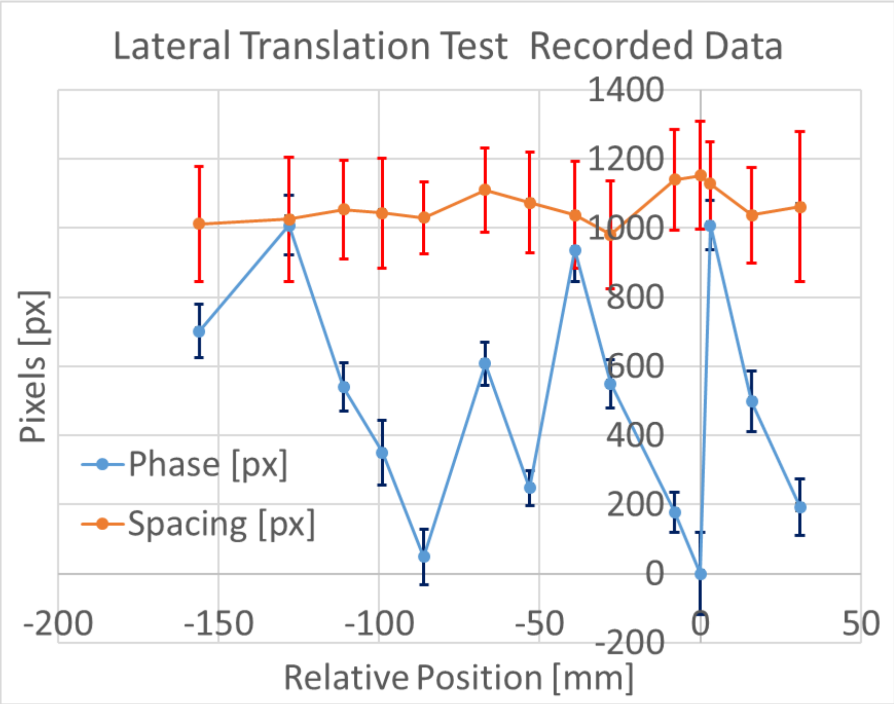

Figure 31: Recorded data from the camera lateral translation estimation test. Showing the measured phase (blue), and spacing (orange) against the relative position.

The accuracy of the model showing the propagated error bars for the camera lateral translation estimations are shown in Figure 32. The plot shows how close the values calculated using Equation 15 are to the real-world values that were recorded. All values are calculated mod p_d as the moiré pattern is periodic in the camera lateral translation by this value. With this setup, p_d is 42 mm. The graph has also been normalised so that values differing by roughly 42 mm are shown as being close estimates. The full calculated values for this figure can be found in Appendix A.

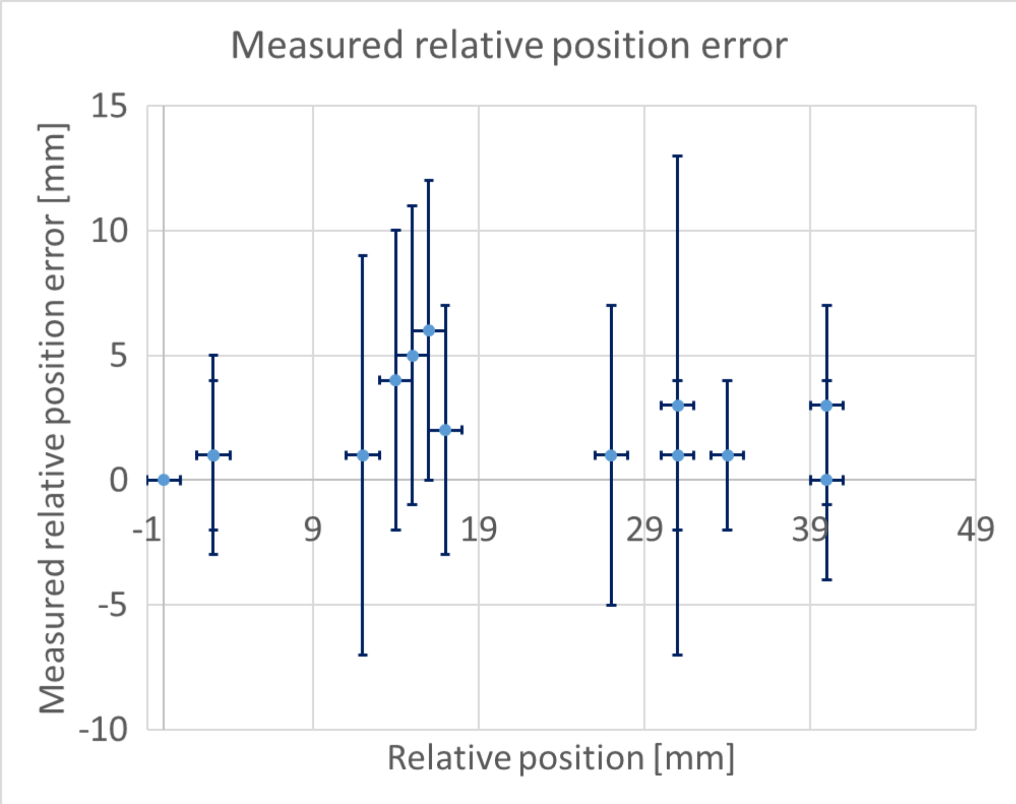

Figure 32: Accuracy of camera lateral translation estimation using the model equation.

Table 4 shows the fixed parameters for the camera distance estimation experiment and their uncertainties. The angle is the counter-clockwise rotation that pattern 1 had in relation to pattern 2, as was shown by Figure 25 and Figure 26.

Table 4: Set parameters for the camera distance estimation experiments.

d **[mm]**	***d*** **error [mm]**	θ_1 **[deg]**	θ_1 **error [deg]**	p_1 **[mm]**	p_2 **[mm]**
90	5	7	1	2	2.1

Figure 33 shows a plot of the recorded data and their error bars from the camera distance estimation experiments. The raw data for this plot can be found in Appendix B. The slope angle is the angle of the moiré pattern fringes in the camera image. This also shows the hyperbolic relationship that is expected by the theory. The slope value was calculated from the measured slope angle in the image.

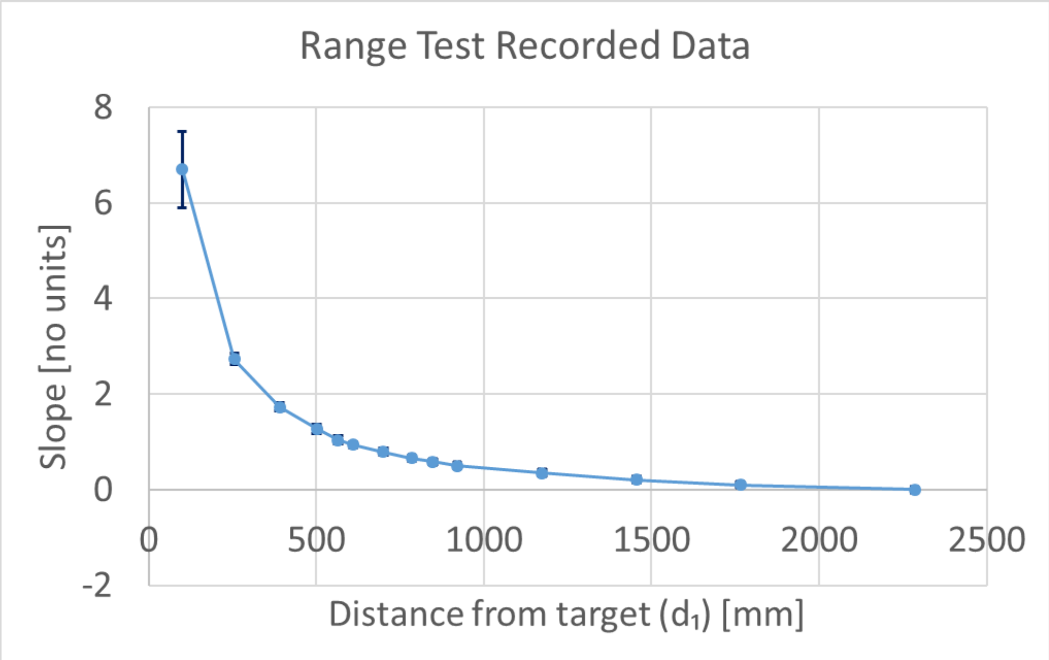

Figure 33: Recorded data from the camera distance estimation experiments.

The accuracy of the model for the camera distance estimation is shown in Figure 34. This shows how close the values calculated by using Equation 12 were to the real-world measurements. Propagated error for this model grows rapidly, so error bars larger than 500 mm have been omitted for clarity. The full calculated values for this figure without the omitted propagated errors can be found in Appendix B.

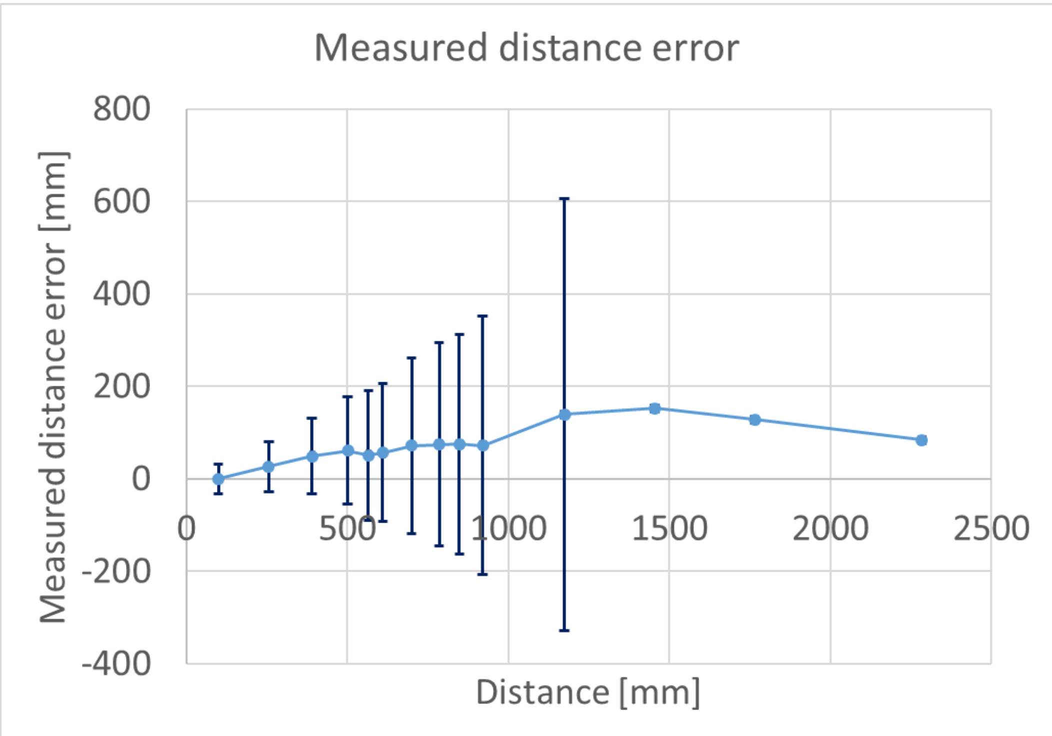

Figure 34: Accuracy of camera distance estimation using the model equation.

4.2. Turntable Tests

Figure 35 shows the results from the −30° to 30° tests, testing the tilt angle estimation accuracy for a wide range. These tests were recorded in courser steps of 1°. The figure shows the maximum, minimum, and average error of the several repeats run at each angle for this test. Each angle represents the turntable's recorded angle when the image was taken before the angle offset calculation to determine the angle relative to the camera's global coordinates. The large spikes are outliers where the solver has found a very close match to the image using a wildly different tilt angle.

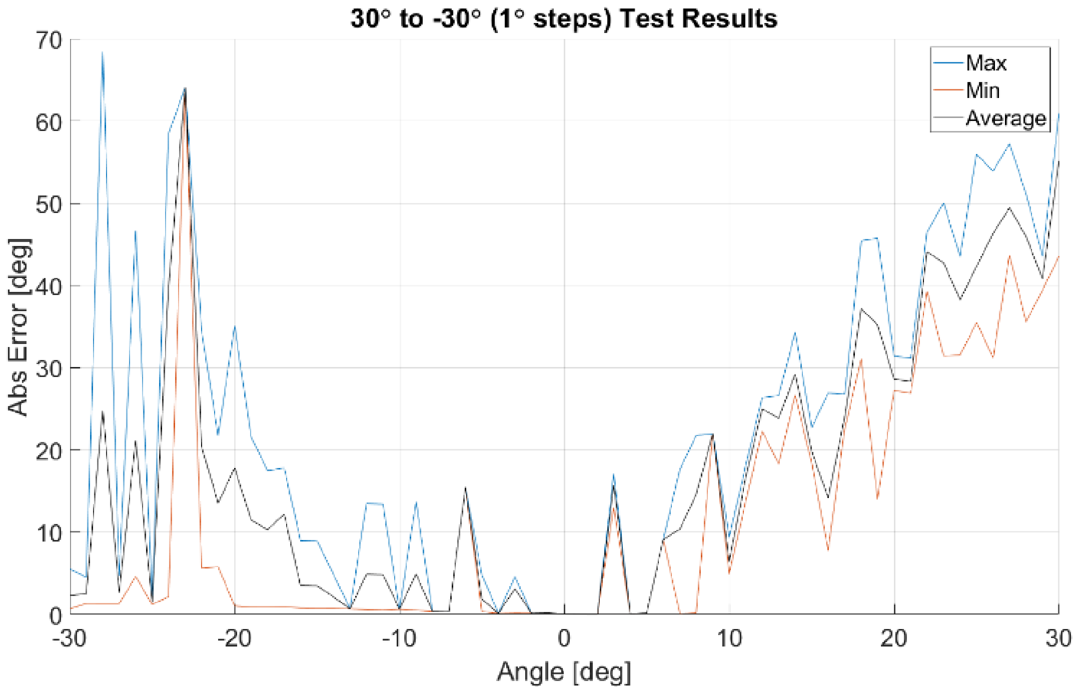

Figure 35: Maximum, minimum, and average estimated angle error for each tilt angle for the −30° to 30° tests.

Figure 36 shows the results from the −5° to 5° tests, testing the tilt angle estimation accuracy for a wide range. These tests were recorded in steps of 0.5°. The figure shows the maximum, minimum, and average error of the several repeats run at each angle for this test.

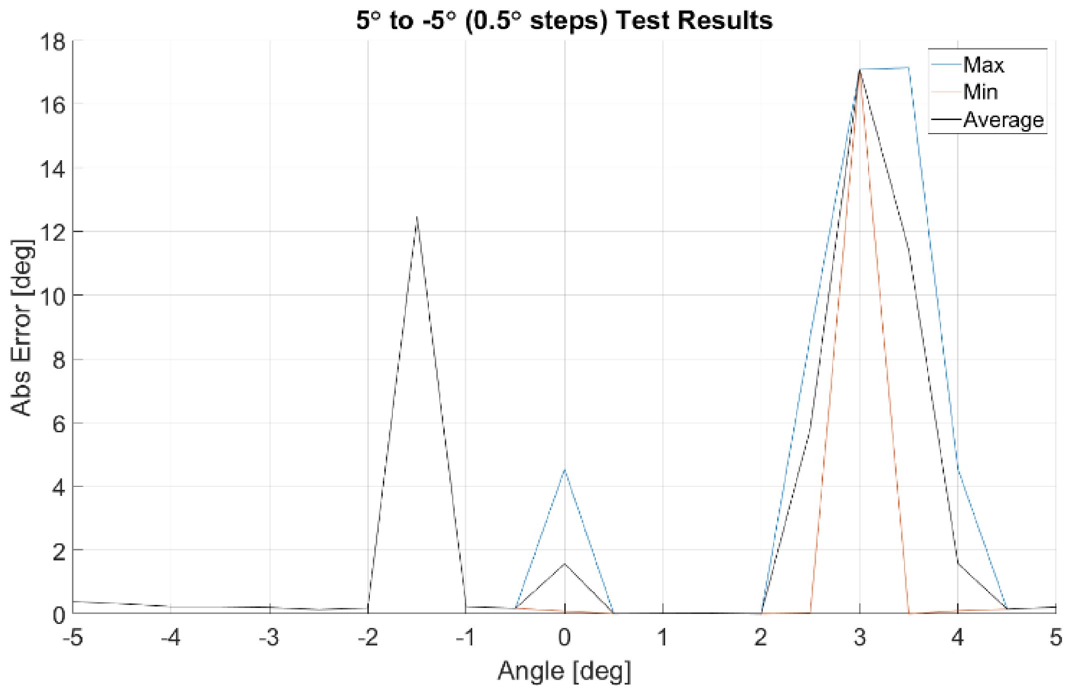

Figure 36: Maximum, minimum, and average estimated angle error for each tilt angle for the $-5°$ to $5°$ tests.

Figure 37 shows the results from the −1° to 1° tests, testing the tilt angle estimation accuracy for a wide range. These tests were recorded in finer steps of 0.1°. The figure shows the maximum, minimum, and average error of the several repeats run at each angle for this test.

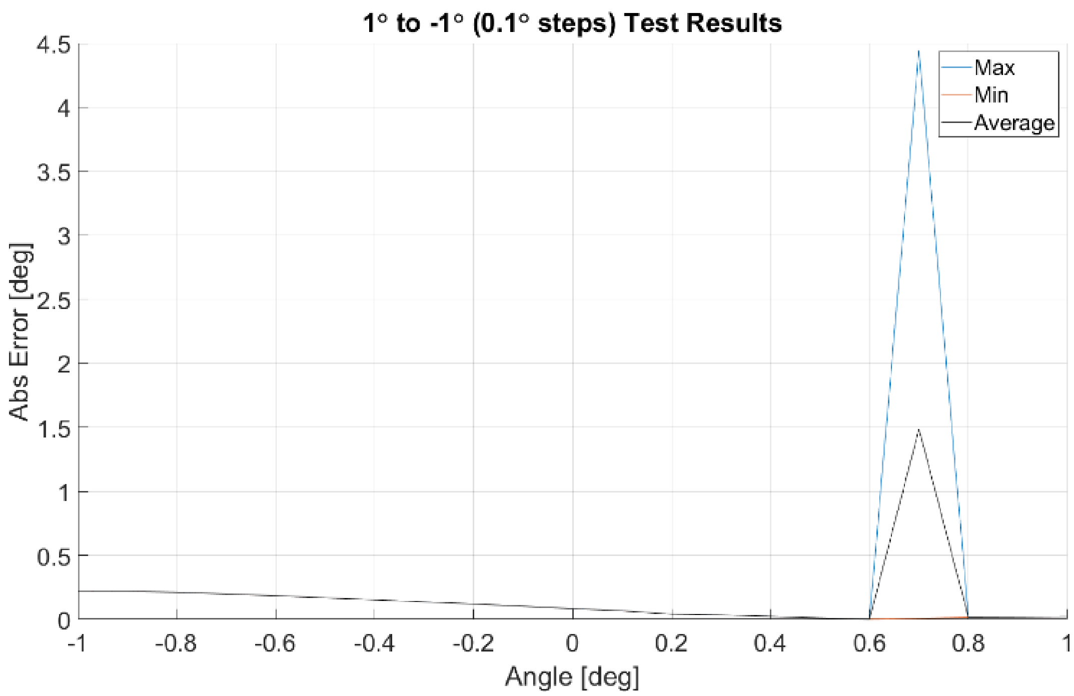

Figure 37: Maximum, minimum, and average estimated angle error for each tilt angle for the $-1°$ to $1°$ tests.

The full raw recorded data for all these experiments can be found in Appendix C.

4.3. Discussion

4.3.1. First Tests

The results from the camera lateral translation experiments appeared to be accurate for the close-range testing. The small separation tested meant that a close range was needed in order to observe shifts in the moiré pattern. However, the issue with this method is it is restricted to estimations mod p_d. This can be countered by trying to design a pattern with a large p_d, i.e. with generating patterns with much closer frequencies. Another solution is to have multiple patterns with varying sensitivities to camera lateral translation, say a moiré pattern with fast-moving fringes and another with slow-moving fringes, and use that to calculate a combined estimation of the camera lateral translation. Alternatively, starting from a known reference, you could try and continuously track the phase changes between frames and estimate the distance that way.

The results from the camera distance experiments showed some promise; however, they weren't nearly as accurate as first anticipated when looking at the propagated errors. Especially at greater distances. This is partly since the model calculation has a suspected singularity point that causes large error propagation near a specific distance. This is since moiré patterns can be so sensitive that minor changes can have growing propagated effects on accuracy with distance. The error bars for this experiment were generous to begin with, however, as these were less precise tests. This is also since it is difficult to ensure that the two generating patterns were perfectly aligned and parallel at the much larger separation distance that was tested, causing unaccounted for errors. The size of the separation distance used is required in order to observe the rotating of the moiré pattern as distance changes; at too small of a separation, the rotating effect becomes less prominent. More accurate results might be observed if these issues can be addressed in future experiments. Due to the less precise nature of these tests, however, they do help get an idea of accuracies you may expect if an average user were to set up a moiré pattern.

4.3.2. Turntable Tests

The most notable thing about the turntable tests is that there were a lot of outlying solutions provided by the solver; especially for the larger range tests, such as the −30° to 30° tests. If these large outliers were removed, it shows a clearer trend of the inaccuracy starting small at around 0.05° error near a 0° angle and growing to around 5° error at –30°. This is best when the initial guess starts near the solution. Since in practice we're likely to use a previously known initial guess (say, from a previous frame of continuous footage), it is not unrealistic to assume this. From the graphs, it tends to also show that the angle estimates for positive angles are way off and continue to grow as the angle gets larger. Looking at these values the solver finds shows that what is going on is that, since positive and negative angle tilts of the moiré pattern look so similar, for positive angles the solver is settling in on the exact opposite negative angle. For example, instead of determining the pattern was at an angle of +12°, it will think it was at about –12° and so the error becomes roughly 24°. This doesn't happen for the negative angles as the solver always favours one side. In one sense it "checks" the negative side of the problem space first before it gets to the positive side, and so it gets lost. Therefore, in this discussion data from positive angles is largely ignored.

When comparing the images of the less accurate estimates (with errors greater than 5°) further from 0° by simulating them visually, they are almost perfectly matched. This suggests that the reason the accuracy gets larger is not the fault of the pattern or the simulator and solver. It is probably due to the many other potential error sources, such as measurement errors, alignment and construction errors, and calibration errors. Measurement errors include errors in taking measurements of the setup, one important one being the distance from the turntable's centre to the camera. Alignment and construction errors include the ability to align and print the grating patterns correctly and accurately when creating the moiré pattern. Ensuring these two patterns are perfectly parallel and that the gratings are aligned is important as moiré patterns are very sensitive to slight variation in construction. The printing of these gratings patterns is also only so accurate. However, in these experiments, the calibration errors were likely the biggest source of error. Specifically, the camera calibration parameters, which were not precisely known. It is predicted that this factor caused majority of the error that appears to increase for larger angles. This effect on accuracy is more prominent for the wider/larger tilt angles, leading to a drift in accuracy caused by the imprecise camera parameters. At these extreme angles of ±30° the moiré pattern is much more sensitive to imperfections in how it is captured. Camera calibration isn't significant for determining estimates of the angle of a moiré pattern from an image, but it is important for comparisons drawn in attempting to profile the accuracy and errors of the experiments run. That is, the angles from the solver are likely more accurate than the calculated reference angles due to not precisely knowing the camera parameters.

This can also help explain the jagged nature and large errors of the data. When the solver is solving for a tilt angle, its initial guess starts near where the measured true solution is. However, if this determined "true solution" itself is not very accurate, then the solver may encounter a different closer local minimum than the one at the true solution. This is amplified by the fact that the moiré pattern used is periodically repeating through its angle sweep. If the pattern were closer, this would be reconcilable due to sharper field of view; however, at longer distances, the effects of perspective are very minimal. This causes the moiré pattern to look very similar at multiple different tilt angles, which effectively creates many periodic local minima across the solution space.

Two ways to attempt to solve this issue using the same type of moiré pattern as used in this test would be to either use the moiré pattern in conjunction with a fiducial marker or two use two or more differently-designed moiré patterns. Using a fiducial marker would provide an initial guess for the moiré solver that was more accurate and already close to the true solution to allow a refinement of the estimate given by the fiducial marker. Of course, an accurate fiducial marker also requires having a calibrated camera. Using two or more moiré patterns of different periods would also help smooth out the solution space and widen out the spacing of local minima that do exist.

5. Conclusion

An investigation into the properties of moiré patterns was carried out. Specifically looking at their potential use in aiding long-range positioning, what the best choice of moiré pattern parameters for a working range is, and if the extra sensitivity of moiré patterns makes greater accuracy patterns more accessible for the average user. It was found, for the lateral translation estimation experiment, the error was about 0.2 mm to 5 mm at a distance of 160 mm. For the distance estimation experiment, the error ranged from about 0 to 180 mm at distances ranging from 100 mm to about 2000 mm. A pattern was designed using the developed theory to choose suitable parameters for a moiré pattern for the application of angle estimation at roughly 3 meters. The more precise turntable experiments performed at 3.116 m on this pattern showed that the angle estimation error was up to 5° off in the best-case excluding outliers. The estimation being particularly accurate for smaller angles less than 5° with an error of less than 0.25°, going as low as 0.05° even in the worst-cases. This is better than similar existing methods such as the Metria Moiré Phase Tracking marker's maximum absolute errors of up to 2.8 mm and 2.1° [37]. This showed that a moiré pattern could be successfully designed for the specified application and that reasonable accuracy is possible in a less precise environment at closer ranges, which would be useable for an average user. This also suggests that much greater accuracies are possible using these markers if they are set up more precisely. One issue here, however, was that the solver used led to several outliers. Another limitation encountered in this research that limits how well the accuracy of the turntable tests could be quantified is that the precise parameters of the camera used were not known, leading to amplified drift in accuracy for extreme angles. There were also many other potential sources of error which can contribute especially for sensitive moiré patterns. These errors include measurement error and construction errors; however, the camera calibration is likely the biggest cause of inaccuracies in the profiling of the accuracy of the moiré pattern.

This research has developed a model specifically for arbitrary planar moiré patterns consisting of grating patterns. This model can theoretically even be used for any type of generating patterns that are representable as functions. It also provides an Object-Oriented MATLAB framework implementation of this model along with a solver. This framework allows the model to be used to generate moiré patterns and their images as well as feed real-world images of moiré patterns to the solver to determine their parameters, provided enough information is given to the solver.

5.1. Future Work

A limited amount of the model's capacity was investigated and tested, as a lot of time went into creating this model and implementing the MATLAB framework. Future work would undergo more extensive testing to investigate what extreme accuracy is possible with these patterns and these models. Along-side this, the solver would be further fine-tuned to be more stable and provide fewer outliers. It would be ideal to investigate how the solver handles estimating more pose information at once, and ideally if it can estimate all pose information given a specific moiré pattern or array of moiré patterns. Although the main goal was to see the application of these patterns for use-cases of that of an average user, higher more detailed and accurate data could still have been useful in drawing some of these conclusions about their use in these applications. Ideally with precisely machined moiré patterns and an accurately calibrated camera. This would also be interesting for determining precisely the best possible accuracies that are possible with these patterns.

A possible long-term goal would also be to create a second kind of solver, a calibration solver, which could take in some video frames of a constructed moiré pattern made in a certain way and then determine the parameters of this moiré pattern to create an easily-made high-accuracy marker. A typical user may construct this pattern by folding a transparent template, and the calibration solver would adjust for the user-error in construction. The regular solver could then be fed this information in making its pose estimates.

Future work could be put towards investigating different kinds of moiré patterns. Such as non-colinear patterns and non-linear patterns as well as other interesting shapes, such as cylindrical or curved patterns. There are many potential pattern types and combinations that could be explored for positioning. The existing model would need to be significantly modified to model such pattern types; however, they could theoretically be simulated numerically using the MATLAB framework if more generating pattern types were created for it, instead of just grating patterns. Ideally, future work would have allowed the model and MATLAB framework to simulate even more types of moiré patterns. Perhaps using the full Fourier moiré theory to get a fuller picture that also encapsulates pattern intensity. Another possibility is that moiré patterns could be purely numerically simulated in the MATLAB framework. This would allow almost arbitrary moiré patterns to be used; however, numeric simulation is more difficult as it does not lend itself as naturally to estimating pose information from real-world images, as the data does not come in the same form. This approach would also be slower to run.

6. References

[1] L. Spillmann, “The perception of movement and depth in moiré patterns,” *Perception,* vol. 22, pp. 287-308, 02/01, 1993.

[2] C. Chiang, “Stereoscopic Moiré Patterns,” *Journal of the Optical Society of America,* vol. 57, no. 9, pp. 1088-1090, 1967/09/01, 1967.

[3] I. Amidror, R. Deriche, and T. S. Huang, *The Theory of the Moiré Phenomenon*, London, UNITED KINGDOM: Springer, 2009.

[4] M. Abolhassani, and M. Mirzaei, “Unification of formulation of moiré fringe spacing in parametric equation and Fourier analysis methods,” *Applied Optics,* vol. 46, no. 32, pp. 7924-7926, 2007/11/10, 2007.

[5] O. Bryngdahl, “Moiré and higher grating harmonics,” *Journal of the Optical Society of America,* vol. 65, no. 6, pp. 685-694, 1975/06/01, 1975.

[6] G. Oster, M. Wasserman, and C. Zwerling, “Theoretical Interpretation of Moiré Patterns,” *Journal of the Optical Society of America,* vol. 54, no. 2, pp. 169-175, 1964/02/01, 1964.

[7] S. Rasouli, and M. T. Tavassoly, “Analysis of the moiré pattern of moving periodic structures using reciprocal vector approach,” *Journal of Physics: Conference Series,* vol. 350, pp. 012032, 2012/03/14, 2012.

[8] M. Yeganeh, and S. Rasouli, “Moiré fringes of higher-order harmonics versus higher-order moiré patterns,” *Applied Optics,* vol. 57, no. 33, pp. 9777-9788, 2018/11/20, 2018.

[9] I. Amidror, and R. D. Hersch, “Mathematical moiré models and their limitations,” *Journal of Modern Optics,* vol. 57, no. 1, pp. 23-36, 2010.

[10] W. W. Skeat, and W. W. Skeat, *The concise dictionary of English etymology*: Wordsworth Editions, 1993.

[11] O. Bryngdahl, “Characteristics of superposed patterns in optics,” *Journal of the Optical Society of America,* vol. 66, no. 2, pp. 87-94, 1976/02/01, 1976.

[12] V. Saveljev, and S.-K. Kim, “Controlled moiré effect in multiview three-dimensional displays: image quality and image generation,” *Optical Engineering,* vol. 57, no. 6, pp. 061623, 2018.

[13] Z. Zhuang, P. Surman, L. Zhang, R. Rawat, S. Wang, Y. Zheng, and X. W. Sun, “Moiré-reduction method for slanted-lenticular-based quasi-three-dimensional displays,” *Optics Communications,* vol. 381, pp. 314-322, 2016.

[14] R. D. Hersch, and S. Chosson, “Band moiré images,” *ACM Trans. Graph.,* vol. 23, no. 3, pp. 239–247, 2004.

[15] A. Luxmoore, and A. Shepherd, “Applications of the moiré effect,” *IN: Optical transducers and techniques in engineering measurement (A84-37276 17-35). London, Applied Science Publishers, 1983, p. 61-108.*, 01/01, 1983.

[16] M. Basehore, and D. Post, “Moiré method for in-plane and out-of-plane displacement measurements,” *Exp. Mech.,* vol. 21, pp. 321-328, 09/01, 1981.

[17] Y. O. Nishijima, Gerald, “Moiré Patterns: Their Application to Refractive Index and Refractive Index Gradient Measurements,” *Journal of the Optical Society of America*, 1964/01/01, 1964.

[18] D. Post, and W. Baracat, “High Sensitivity Moiré Interferometry–A Simplified Approach,” *Experimental Mechanics,* vol. 21, pp. 100-104, 03/01, 1981.

[19] P. Y. Chen, X. Q. Zhang, Y. Y. Lai, E. C. Lin, C. A. Chen, S. Y. Guan, J. J. Chen, Z. H. Yang, Y. W. Tseng, S. Gwo, C. S. Chang, L. J. Chen, and Y. H. Lee, “Tunable Moiré Superlattice of Artificially Twisted Monolayers,” *Advanced Materials,* vol. 31, no. 37, pp. e1901077-n/a, 2019.

[20] H. Takasaki, “Moiré Topography,” *Japanese Journal of Applied Physics,* vol. 14, pp. 441, 01/01, 1975.

[21] O. N. Kuzyakov, U. V. Lapteva, and M. A. Andreeva, “Electronic-projecting Moire method applying CBR-technology,” *Journal of Physics: Conference Series,* vol. 944, pp. 012072, 2018/01, 2018.

[22] P. Balla, G. Manhertz, and A. Antal, “Diagnostic moiré image evaluation in spinal deformities,” *Optica Applicata,* vol. 46, no. 3, 2016.

[23] M. Wijk, “Moiré Contourgraphs — An Accuracy Analysis,” *Journal of biomechanics,* vol. 13, pp. 605-13, 02/01, 1980.

[24] A. Livnat, and O. Kafri, “Moire pattern of a linear grid with a lenticular grating,” *Optics letters,* vol. 7, no. 6, pp. 253-255, 1982.

[25] A. Moldagalieva, D. Fadeyev, A. Kuzdeuov, V. Khan, B. Alimzhanov, and H. A. Varol, "Computer Vision-Based Pose Estimation of Tensegrity Robots Using Fiducial Markers." pp. 478-483, 2019.

[26] B. Armstrong, T. Verron, L. Heppe, J. Reynolds, and K. Schmidt, "RGR-3D: simple, cheap detection of 6-DOF pose for teleoperation, and robot programming and calibration." pp. 2938-2943 vol.3, 2002.

[27] S. Siltanen, “Theory and applications of marker based augmented reality,” 2012.

[28] H. Kato, and M. Billinghurst, "Marker tracking and HMD calibration for a video-based augmented reality conferencing system." pp. 85-94, 1999.

[29] D. Wagner, and D. Schmalstieg, “ARToolKitPlus for pose tracking on mobile devices,” 2007.

[30] M. Fiala, “ARTag revision 1, a fiducial marker system using digital techniques,” *National Research Council Publication,* vol. 47419, pp. 1-47, 2004.

[31] E. Olson, "AprilTag: A robust and flexible visual fiducial system." pp. 3400-3407.

[32] M. J. Edwards, M. P. Hayes, and R. D. Green, "High-accuracy fiducial markers for ground truth." pp. 1-6, 2016.

[33] H. Tanaka, K. Ogata, and Y. Matsumoto, "Solving pose ambiguity of planar visual marker by wavelike two-tone patterns." pp. 568-573, 2017.

[34] I. Rabbi, and S. Ullah, “Extending the Tracking Distance of Fiducial Markers for Large Indoor Augmented Reality Applications,” *Advances in Electrical and Computer Engineering,* vol. 15, pp. 59-64, 05/31, 2015.

[35] H. Tanaka, Y. Sumi, and Y. Matsumoto, "Application of moiré patterns to AR markers for high-accuracy pose estimation," 2012.

[36] H. Tanaka, Y. Sumi, and Y. Matsumoto, "A visual marker for precise pose estimation based on lenticular lenses." pp. 5222-5227, 2012.

[37] K. Gumus, B. Keating, N. White, B. Andrews-Shigaki, B. Armstrong, J. Maclaren, M. Zaitsev, A. Dale, and T. Ernst, “Comparison of optical and MR-based tracking,” *Magnetic resonance in medicine,* vol. 74, no. 3, pp. 894-902, 2015.

[38] B. S. Armstrong, T. Verron, L. A. Heppe, R. M. Karonde, J. Reynolds, and K. Schmidt, “RGR-6D: low-cost, high-accuracy measurement of 6-DOF pose from a single image,” *Milwaukee (WI): Manuscript, University of Wisconsin*, 2007.

[39] I. Amidror, and R. D. Hersch, “The role of Fourier theory and of modulation in the prediction of visible moiré effects,” *Journal of Modern Optics,* vol. 56, no. 9, pp. 1103-1118, 2009/05/20, 2009.

[40] M. M. Hasan, “Analytical Study for Phase Extraction Algorithm of Moire Fringe based Sensing System,” 2013.

[41] K. Patorski, S. Yokozeki, and T. Suzuki, “Moiré Profile Prediction by Using Fourier Series Formalism,” *Japanese Journal of Applied Physics,* vol. 15, no. 3, pp. 443-456, 1976/03, 1976.

[42] M. I. A. Lourakis. "Levenberg-Marquardt Nonlinear Least Squares Algorithms in C/C++," April 29, 2020; www.ics.forth.gr/~lourakis/levmar/.

7. Appendices

7.1. Appendix A – Lateral Translation Tests

7.1.1. Raw Data

Table 5 shows the raw recorded data and their uncertainties from the experiments performed to test the camera lateral translation estimation. The relative position given is the position relative to the measured position that was retroactively determined to be the zero-point. The zero-point corresponds to when a fringe is centred directly down the centre of the camera image in order to match up with the assumptions of the theory.

Table 5: Recorded data from the camera lateral translation estimation test.

Measured position [mm]	Relative position [mm]	Relative position error [mm]	Phase [px]	Phase error [px]	Spacing [px]	Spacing error [px]
-103	-156	1	702	77	1012	166
-75	-128	1	-18	86	1026	180
-58	-111	1	540	70	1054	143
-46	-99	1	350	94	1044	159
-33	-86	1	48	81	1030	105
-14	-67	1	608	62	1110	123
0	-53	1	248	51	1074	147
14	-39	1	-102	92	1038	155
25	-28	1	-432	71	981	156
46	-8	1	178	58	1140	146
53	0	1	0	120	1152	156
56	3	1	-120	72	1128	123
69	16	1	-540	88	1038	138
84	31	1	-870	82.5	1062	218

7.1.2. Calculations

The results of the calculations and the propagated uncertainties for the camera lateral translation estimations are shown in Table 6. These are calculated using Equation 15 using the data from Table 5. Everything is calculated mod p_d as the moiré pattern is periodic in the camera lateral translation estimation by this value. Here p_d is 42 mm. Also, note that this implies that values differing by roughly 42 mm are close values.

Table 6: Camera lateral translation calculations using the model equation.

Mod relative position [mm]	**Relative position error [mm]**	**Mod calculated position [mm]**	**Mod calculated position error [mm]**
12	1	13	8
40	1	1	4
15	1	20	6
27	1	28	6
40	1	40	4
17	1	19	5
31	1	32	3
3	1	4	4
14	1	18	6
34	1	35	3
0	1	0	-
3	1	4	3
16	1	22	6
31	1	34	10

7.2. Appendix B – Distance Tests

7.2.1. Raw Data

Table 7 shows the recorded data and their uncertainties from the camera distance estimation experiments. The slope angle is the gradient angle of the moiré pattern fringes in the camera image. The slope value was calculated from the measured slope angle in the image.

Table 7: Recorded data from the camera distance estimation experiments.

d_1 [mm]	d_1 error [mm]	Slope angle [deg]	Slope angle error [deg]	Slope	Slope error
100	2	81.5	1.0	6.70	0.80
256	2	69.9	0.8	2.73	0.12
390	5	59.9	1.2	1.73	0.08
501	5	51.8	1.9	1.27	0.09
565	5	46.2	2.3	1.04	0.08
610	5	43.2	2.2	0.94	0.07
700	5	38.2	3.0	0.79	0.08
785	8	33.3	2.9	0.66	0.07
848	8	30.2	2.8	0.58	0.06
920	8	26.8	2.6	0.50	0.06
1174	10	19.4	3.3	0.35	0.07
1455	10	12.0	3.3	0.21	0.06
1765	10	5.6	2.7	0.10	0.05
2285	10	-0.5	2.3	-0.01	0.04

7.2.2. Calculations

The results from the camera distance estimation and the propagated uncertainties are shown in Table 8. These were calculated using Equation 12 using the data in Table 7.

Table 8: Results from camera distance estimation experiments.

Calculated distance [mm]	Distance error [mm]
100	32
230	54
341	81
440	116
514	140
554	149
628	190
711	220
773	237
848	280
1035	467
1303	787
1637	1658
2201	18134

7.3. *Appendix C – Turntable Tests*

The following shows the raw data of the estimated angle results calculated from the model and optimisation solver for each of the turntable tests. The wide-angle variation test tested a range of −30° to 30° with steps of 1°; the small-angle variation test tested a range of −5° to 5° with steps of 0.5°; and the narrow-angle variation test testing a range of −1° to 1° with steps of 0.1°.

7.3.1. *Wide-Angle Variation Test*

Table 9 shows the raw data of the estimated angle results for the −30° to 30° test with steps of 1°.

Table 9: Table of raw data from the solver for the −30° to 30° test.

True Angle	Initial Guess 1	Initial Guess 2	Initial Guess 3
-35.05	-35.75	-35.75	-29.53
-34.05	-35.74	-29.52	-32.74
-33.05	35.39	-28.47	-31.75
-32.05	-33.95	-27.33	-30.75
-31.05	15.59	-26.45	-19.01
-30.05	-32.11	-28.85	-28.85
-29.05	-31.22	29.42	29.42
-28.05	36.00	36.00	36.00
-27.05	-32.67	-5.94	7.45
-26.05	-31.83	-4.32	-12.98
-25.05	10.02	-24.01	-7.67
-24.05	-36.00	-2.44	-23.16
-23.05	-35.59	-22.16	-5.55
-22.05	-4.22	-4.22	-21.12
-21.05	-12.07	-20.25	-20.25
-20.05	-11.12	-19.29	-19.29
-19.05	-14.19	-18.28	-18.28
-18.05	-17.37	-17.37	-17.37
-17.05	-16.45	-3.55	-16.45
-16.05	-15.50	-2.63	-15.50
-15.05	-14.41	-14.41	-14.41
-14.05	-0.37	-13.52	-13.52
-13.05	-12.66	-12.66	-12.66
-12.05	-11.70	-11.70	-11.70
-11.05	-26.49	-26.49	-26.49
-10.05	-9.67	-9.67	-5.26
-9.05	-8.90	-8.90	-8.90

-8.05	-3.45	-3.45	-7.85
-7.05	-6.87	-6.87	-6.87
-6.05	-5.83	-5.83	-5.83
-5.05	-4.97	-4.97	-4.97
-4.05	-4.07	-4.07	-4.07
-3.05	-3.06	-3.06	-3.06
-2.05	-15.05	-19.14	-19.14
-1.05	-1.15	-1.15	-1.15
-0.05	-0.26	-0.26	-0.26
0.95	-8.16	-8.16	-8.16
1.95	1.84	-11.44	-15.67
2.95	-18.83	2.73	-18.83
3.95	-18.01	-18.01	-18.02
4.95	0.03	-4.41	0.03
5.95	-12.16	-7.82	-12.16
6.95	-19.41	-19.37	-15.32
7.95	-18.68	-18.68	-10.33
8.95	-25.34	-17.70	-17.70
9.95	-8.44	-12.75	-8.44
10.95	18.73	18.73	-15.98
11.95	-10.58	-10.58	-14.83
12.95	-18.11	-32.49	-22.06
13.95	-31.79	-31.79	-0.05
14.95	-12.27	-12.27	-16.45
15.95	-10.95	-10.95	-15.22
16.95	-29.54	-29.54	-22.35
17.95	-32.08	-28.78	-13.47
18.95	-24.52	-12.57	-20.74
19.95	-15.53	-15.53	-36.00
20.95	-10.26	-32.93	-32.90
21.95	-25.43	-35.28	-21.70
22.95	-28.16	-28.16	-12.63
23.95	-15.47	-15.47	-19.57
24.95	-35.96	-35.96	-18.59

7.3.2. Small-Angle Variation Test

Table 10 shows the raw data for the estimated angles results from the –5° to 5° tests with 0.5° steps.

Table 10: Table of raw data from the solver for the −5° to 5° test.

True Angle	Initial Guess 1	Initial Guess 2	Initial Guess 3
-10.05	-9.67	-9.67	-9.67
-9.55	-9.24	-9.24	-9.24
-9.05	-8.83	-8.83	-8.83
-8.55	-8.33	-8.33	-8.33
-8.05	-7.85	-7.85	-7.85
-7.55	-7.42	-7.42	-7.42
-7.05	-6.87	-6.87	-6.87
-6.55	-19.02	-19.02	-19.02
-6.05	-5.83	-5.83	-5.83
-5.55	-5.38	-5.38	-5.38
-5.05	-4.97	-0.52	-4.97
-4.55	-4.54	-4.54	-4.54
-4.05	-4.07	-4.07	-4.07
-3.55	-3.58	-3.58	-3.58
-3.05	-3.05	-3.05	-3.05
-2.55	-11.29	-11.29	-2.51
-2.05	-19.13	-19.13	-19.13
-1.55	-1.55	-18.69	-18.69
-1.05	-5.59	-1.15	-1.15
-0.55	-0.69	-0.69	-0.69
-0.05	-0.26	-0.26	-0.26

7.3.3. Narrow-Angle Variation Test

Table 11 shows the raw data for the estimated angles results from the –5° to 5° tests with 0.5° steps.

Table 11: Table of raw data from the solver for the −1° to 1° test.

True Angle	Initial Guess 1	Initial Guess 2	Initial Guess 3
-6.05	-5.83	-5.83	-5.83
-5.95	-5.73	-5.73	-5.73
-5.85	-5.64	-5.64	-5.64
-5.75	-5.55	-5.55	-5.55
-5.65	-5.46	-5.46	-5.46
-5.55	-5.38	-5.38	-5.38
-5.45	-5.3	-5.3	-5.3
-5.35	-5.21	-5.21	-5.21
-5.25	-5.13	-5.13	-5.13
-5.15	-5.05	-5.05	-5.05
-5.05	-4.97	-4.97	-4.97
-4.95	-4.88	-4.88	-4.88
-4.85	-4.81	-4.81	-4.81
-4.75	-4.71	-4.71	-4.71
-4.65	-4.63	-4.63	-4.63
-4.55	-4.54	-4.54	-4.54
-4.45	-4.45	-4.45	-4.45
-4.35	0.09	-4.36	-4.36
-4.25	-4.27	-4.27	-4.27
-4.15	-4.17	-4.17	-4.17
-4.05	-4.07	-4.07	-4.07